

Tuning the magnetic and structural properties of Fe₃O₄ films grown on Nb: SrTiO₃ substrates

Master thesis of

Yifan Xu

At the Jülich Center for Neutron Science,
Institute of Quantum Materials and Collective Phenomena
in Forschungszentrum Jülich

Supervisor:	Prof. Dr. Thomas Brückel
Second supervisor:	Prof. Dr. Regina Dittmann
Advisor:	Dr. Mai Hussein Hamed Dr. Connie Bednarski-Meinke

4. January 2022 – 4. July 2022

Contents

Abstract	viii
Überblick	ix
Acknowledgements	x
1 Introduction	1
2 Theory	3
2.1 Iron oxide	4
2.1.1 Magnetite (Fe_3O_4)	4
Structure	4
Properties	4
Verwey transition	6
2.1.2 Wüstite (Fe_{1-x}O)	7
2.1.3 Maghemite ($\gamma\text{-Fe}_2\text{O}_3$)	8
2.1.4 Hematite ($\alpha\text{-Fe}_2\text{O}_3$)	8

2.2	Oxide substrate: SrTiO ₃	9
2.2.1	SrTiO ₃ crystal structure	9
2.2.2	Epitaxial growth of Fe ₃ O ₄ on STO substrates	10
	Antiphase boundaries (APBs)	10
2.2.3	Gibbs free energy	10
3	Experimental methods	12
3.1	Pulsed laser deposition (PLD)	12
3.2	Atomic force microscopy (AFM)	13
3.3	X-Ray Reflectometry/ Diffractometry (XRR and XRD)	14
3.4	Vibrating sample magnetometer (VSM)	16
3.5	Magnetic properties measurement system (MPMS)	17
3.6	Wide-Angle X-ray Scattering (WAXS)	19
3.7	Reciprocal space mapping (RSM)	20
4	Growth optimization of Fe₃O₄/STO	23
4.1	Substrate preparation	23
4.2	AFM	23
4.3	XRR	25
4.4	XRD	26
4.5	WAXS	29
4.6	VSM	32

4.6.1	Saturation magnetization	32
4.6.2	Coercivity and remanence magnetization	34
4.6.3	Verwey transition	35
4.7	Conclusion	37
5	Tuning the properties of thin films by electric field: in-situ SQUID	39
5.1	Magnetization tuned by an electric field	39
5.2	Structure tuned by electric field: ex-situ XRD	42
6	Summary	45
7	Outlook	47
A	The calculation of WAXS data	49
B	Sources of systematic error in the WAXS system	52
	Bibliography	55

List of Figures

2.1	Unit cell of three different phases of iron oxide drawn by VESTA	3
2.2	The different interactions in the inverse spinel structure drawn by VESTA: (a) the antiferromagnetic superexchange interaction, (b) the ferromagnetic superexchange interaction, and (c) the ferromagnetic double-exchange interaction	6
2.3	Verwey temperature for different oxygen content (figure taken from [1])	7
2.4	The unit cell of different substrate: (a) STO and (b) YSZ	9
3.1	Sketch of PLD process	13
3.2	Principle of AFM measurement	14
3.3	Sketch of D8 XRR (figure taken from ref. [2])	15
3.4	Reflection and refraction of X-ray	15
3.5	Constructive interference in a single thin film system	16
3.6	Bragg's law	17
3.7	VSM coil set and linear transporter (figure taken from ref. [3])	18
3.8	Sample connected with SQUID holder by copper wire	19
3.9	Sketch of GALAXI platform (figure taken from [4])	20

3.10	Sketch of the diffraction process in WAXS	21
3.11	Illustration of diffraction using Ewald's sphere	22
4.1	Treatment to Nb: STO substrate: (a) original substrate, (b) substrate after etching in HF for 1min and (c) substrate after etching and then annealed at 950°C for 2 h	24
4.2	5x5 μm AFM images of (a)Nb: STO substrate and Fe ₃ O ₄ thin films grown on Nb: STO substrates at the growth temperature of (b)400°C, (c)450°C, (d)500°C, (e)550°C and (f)600°C	24
4.3	(a) X-ray reflectivity of samples grown at different temperatures, (b)surface roughness of films calculated from XRR	26
4.4	Out-of-plane X-ray diffraction scans of Fe ₃ O ₄ thin films grown at different temperatures of (a) all reflection in the range of $2\theta=10^\circ-100^\circ$ and (b) Fe ₃ O ₄ (004) reflection in the range of $2\theta=40^\circ-50^\circ$. (c) the out-of-plane lattice constant c_{oop} with different force regions: I) tensile strain, II) relaxed growth and III) compressive strain.	27
4.5	Sketches of Fe ₃ O ₄ crystal unit cells on STO in different situations: I) tensile strained, II) relaxed and III) compressive strained.	28
4.6	The mounting of samples in the WAXS holder	29
4.7	Peak fitting and RSM for samples grown at 400 and 550°C	30
4.8	In-plane and out-of-plane lattice constant calculated from WAXS and XRD	31
4.9	Magnetization versus magnetic field Hysteresis for Fe ₃ O ₄ thin films on Nb: STO substrates at the different growth temperature	33
4.10	(a) Coercive field H_C and (b) remanant magnetization M_r for Fe ₃ O ₄ films grown at different growth temperatures and measured at different temperatures.	34

4.11	(a)-(e): the magnetization versus temperature curves and (f) the Verwey transition temperature calculated from the curves for Fe_3O_4 films grown at different temperature	36
4.12	Magnetization properties of Fe_3O_4 thin films grown at different temperatures calculated from $M(T)$ ZFC curve.	37
5.1	ZFC curves (a)original, (b)repeated, and (c) Verwey transition temperature of sample grown under 600°C with applying different voltage	40
5.2	The sketch of $\text{Fe}_3\text{O}_4/\text{TiO}_2$ -terminated Nb: STO with applying (a)positive voltage and (b) negative voltage	41
5.3	ZFC, 1st and 2nd Derivation with applying -6V for (a)the first time and (b) the second time	42
5.4	(a)ZFC&FC curves and (b) Verwey transition temperature of sample grown under 450°C and (c) ZFC&FC curves when $T_{\text{growth}}=550^\circ\text{C}$ with applying different voltage	43
5.5	XRD images of $\text{Fe}_3\text{O}_4/\text{STO}$ before and after applying voltage in SQUID of samples grown at (a) 450°C , (b) 550°C , and (c) 600°C	44
7.1	Different termination of STO substrate, figure taken from [5]	47
A.1	Sample mounted in WAXS with $\text{PSR}=90^\circ$, $\omega_0=0^\circ$	49
B.1	5 possible sources of error in WAXS system	52
B.2	Intensity integrated of all 2θ over ω	53

List of Tables

- | | | |
|-----|--|----|
| 2.1 | Structure, magnetic and electric properties of iron oxide phases | 8 |
| 2.2 | Gibbs free energy of the iron oxide and the oxide substrates calculated from the database at room temperature based on the data from [6] . . . | 11 |

Abstract

Tuning magnetic oxide phases via redox reactions across their heterointerfaces makes them useful for spintronic and memristive device applications. With controlled film-substrate interfaces and using a small electric field, oxidation/reduction reaction occurs which leads to a reversible phase transition in the thin film. In this work, we achieve magnetic switching of $\text{Fe}_3\text{O}_4/\text{Nb: SrTiO}_3$ heterostructures by applying an electric field. We grow Fe_3O_4 films with different growth temperatures by pulsed laser deposition. The quality of the magnetite films is checked by different techniques e.g. Atomic force microscopy (AFM), X-ray reflectometry (XRR), X-ray diffraction (XRD), and wide angle X-ray scattering (WAXS). Using magnetometry, we detect the Verwey transition which is a strong indicator of the oxygen content in the Fe_3O_4 films. We observe a strong change in the Verwey transition with an applied electric field. This can be explained by oxygen diffusion through the interface which leads to a reversible phase transition from Fe_3O_4 (magnetite) to $\gamma\text{-Fe}_2\text{O}_3$ (maghemite). Additionally, we investigate the structural transitions using ex-situ XRD.

Überblick

Die Steuerung magnetischer Oxidphasen durch Redoxreaktionen über ihre Heterogrenzflächen hinweg ermöglicht die Verwendung dieser Materialien in Spintronik- und memristiven Bauelementen. Bei kontrollierten Film-Substrat-Grenzflächen und eines kleinen elektrischen Feldes tritt eine Oxidations-/Reduktionsreaktion auf, die zu einem reversiblen Phasenübergang führt. In dieser Arbeit erreichen wir magnetisches Schalten von $\text{Fe}_3\text{O}_4/\text{Nb}:\text{SrTiO}_3$ -Heterostrukturen durch Anlegen eines elektrischen Feldes. Wir wachsen Fe_3O_4 Filme mit unterschiedlichen Wachstumstemperaturen durch gepulste Laserabscheidung. Die Qualität der Magnetitfilme wird durch verschiedene Techniken überprüft, z.B. Rasterkraftmikroskopie (AFM), Röntgenreflektometrie (XRR), Röntgenbeugung (XRD) und Weitwinkel-Röntgenstreuung (WAXS). Mittels Magnetometrie detektieren wir den Verwey-Übergang, der ein starker Indikator für den Sauerstoffgehalt in den Fe_3O_4 -Filmen ist. Wir beobachten eine starke Änderung des Verwey-Übergangs mit angelegtem elektrischem Feld. Dies kann durch Sauerstoffdiffusion durch die Grenzfläche erklärt werden, die zu einem reversiblen Phasenübergang von Fe_3O_4 (Magnetit) zu $\gamma\text{-Fe}_2\text{O}_3$ (Maghemit) führt. Darüber hinaus untersuchen wir die Strukturübergänge mit XRD.

Acknowledgments

My deepest gratitude goes first and foremost to Prof. Dr. Thomas Brückel, my main supervisor, for giving me the chance to work at the "Jülich Center for Neutron Science (JCNS-2), Forschungszentrum Jülich GmbH" and instructive suggestions on my thesis. I am thankful to Prof. Dr. Regina Dittmann for being willing to be my second main supervisor and for the useful suggestions.

I am profoundly grateful to Dr. Mai Hussein and Dr. Connie Bednarski-Meinke for being my supervisors, for the constant encouragement and guidance, for imparting me with plenty of knowledge and expertise, for the English language corrections and for walking me through all the stages of the writing of this thesis. The completion of this thesis would not have been possible without their patient instruction, insightful criticism and expert guidance.

My sincere thanks go to Dr. Emmanuel Kentzinger, Dr. Oleg Petravic, Dr. Shibabrata Nandi, Dr. Ulrich Rücker and Berthold Schmitz for the introduction to and suggestions for the devices used throughout this thesis project. My special thanks go to Dr. Asmaa Qdemat, Dr. Patrick Schömann and Thomas Jansen for the helping to conduct the measurements.

I would like to express my heartfelt gratitude to Prof. Karen Friese, Dr. Felix Gunkel and Dr. Annika Stellhorn for the useful discussion.

I would also like to thank all my other colleagues at JCNS-2, especially the thin film group, who are always polite and willing to help and always create a creative and delightful working atmosphere.

Last but not least, my greatest thanks would go to my beloved family, Mr. Hong Xu and Mrs. Huimin Tian and my boyfriend, Mr. Julian Lindlar, have always been supportive of me, and have constantly motivated and encouraged me during my work. I also owe

my sincere gratitude to my friends for their loving consideration of me.

Chapter 1

Introduction

For different phases, iron oxide has variable crystal structures, magnetic properties, and conductance. Half metallic means metallic for one-spin direction and insulating for the other spin direction. Fe_3O_4 is a typical half-metal magnetic material. Additionally, Fe_3O_4 has a high Curie temperature of around 860K allowing it to be used at room temperature. The oxidized phase, $\gamma\text{-Fe}_2\text{O}_3$, has a similar crystal structure with only a slight difference of lattice constant and it is an insulator. The reduced phase, FeO, has a rock salt crystal structure with antiferromagnetism (the details of which will be discussed in Chapter 2) [7]. Thus, we can tune the properties of the thin film by tuning the iron oxide phase.

In order to control the oxygen migration between thin films and substrates, TiO_2 -terminated STO is chosen to be the substrate. The oxygen vacancy inside TiO_2 -terminated STO allows oxygen migration. The lattice mismatch of Fe_3O_4 on STO is around -7.5%. As a result, the growth parameters of Fe_3O_4 are critical, because they can influence its stoichiometry and thus its magnetic properties. Thus, the influence of the growth temperature on the quality of Fe_3O_4 is studied. After the growth optimization, we tried to tune the properties of thin films by applying an electric field. As different iron oxides have different properties, we observe the magnetization change of thin films by applying different voltage. Further, with the help of ex-situ XRD, the structural change can be studied.

In chapter 2 the scientific background of different iron oxides will be introduced. Additionally, the important phenomenon – Verwey transition - will be discussed, which is a good indicator of the oxygen stoichiometry. Also, we introduce the lattice structure and oxygen conducting properties of Nb: SrTiO_3 substrates. The experimental methods

and instruments used for the deposition, characterization, and tuning the properties of the thin films will be introduced in chapter 3. The influence of growth temperature on the properties of Fe_3O_4 thin films on Nb: STO substrate will be discussed in chapter 4; where we analyze the quality, structure and magnetization of the thin films. Finally, the tuning of iron oxide with applied electric field is introduced in chapter 5. We observe the phase change by applying an electric field in the SQUID system and the further structural change using XRD. In chapter 6, we summarize the outcomes of this study. The direction of the further study is discussed in chapter 7.

Chapter 2

Theory

The aim of this thesis is to investigate the properties of Fe_3O_4 thin films on Nb:SrTiO₃ substrates, controlling and tuning the properties of thin films. Therefore, we will introduce the theoretical background in this chapter. In section 2.1, we will introduce the properties of different iron oxide phases particularly magnetite (Fe_3O_4). In section 2.2, the structure and the influence of Nb:SrTiO₃ substrates on the thin films will be introduced.

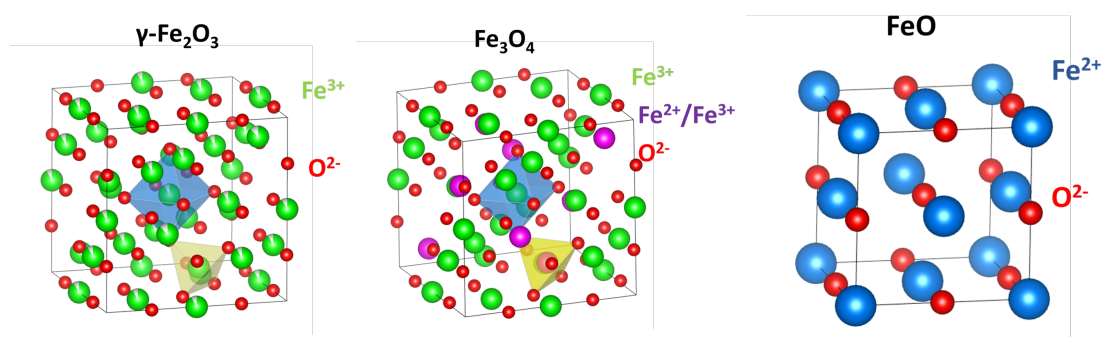


Figure 2.1: Unit cell of three different phases of iron oxide drawn by VESTA

2.1 Iron oxide

Iron oxides (Fe_xO_y) have a wide range of electric and magnetic properties. The properties of thin films can be controlled by phase transitions between different iron oxide phases. Thus we will introduce the different crystal structure and properties of the thin film material Fe_3O_4 , reduced phase Fe_{1-x}O and the oxidized phase Fe_2O_3 .

2.1.1 Magnetite (Fe_3O_4)

Magnetite Fe_3O_4 is a ferrimagnetic half-metal [8]. Half metallic means metallic for one-spin direction and insulating for the other spin direction. Such materials have the density of states of one spin direction near the Fermi level, but a gap in the density of state for the other spin direction. Theoretically we can have 100% polarization near Fermi level [9]. Fe_3O_4 has a high Curie temperature of $T_C=860\text{K}$. Above T_C , magnetite will lose the ferrimagnetic properties and the spin aligned randomly. The high Curie temperature allows it to be used in electronic or spintronic devices at room temperature. “Ferrimagnetic” refers to a spontaneous magnetization caused by the different ions Fe^{2+} and Fe^{3+} which are unequal in magnitude. The special properties of Fe_3O_4 originating from the crystal structure will be introduced. Moreover, the characteristic metal-insulator transition of Fe_3O_4 around the Verwey transition of 120K will be introduced.

Structure

Fe_3O_4 has a cubic inverse spinel structure, with a crystal lattice constant of 8.394 \AA , as shown in fig.2.1. The octahedral sites are occupied by both Fe^{2+} and Fe^{3+} cations while the tetrahedral sites are only occupied by Fe^{3+} . The pattern of occupation of Fe^{2+} and Fe^{3+} cations causes the special ferrimagnetic and electric properties of magnetite as the sublattice with an opposite orientation of the magnetic moment.

Properties

Exchange interaction is important for the long range magnetic order. Driven to conserve kinetic energy, the electrons tend to wander around both atoms rather than just one by

forming bonds, and this is exchange interaction. There are different kinds of exchange. The direct exchange is via a direct overlap between neighbouring magnetic orbitals. Between magnetic cations Fe^{2+} and Fe^{3+} , there is not only direct exchange but also the indirect exchange [10]. The different ways of indirect coupling can be defined as superexchange and double-exchange interaction and are shown in fig.2.2, respectively.

Superexchange Superexchange is the coupling of two cations through a non-magnetic anion [11] [12] [13]. It is caused by the overlap of the cation d-orbitals and the oxygen p-orbitals. Most of superexchange interaction is antiferromagnetic. Antiferromagnetic coupling lowers the energy by delocalizing the electrons over the whole structure [10]. It depends on the overlap of the orbitals and thus, is highly dependent on the angle between bonds. Superexchange can also be weak ferromagnetic in some circumstances, which is described by the Goodenough-Kanamori rules [13]:

Antiferromagnetic coupling originates from 180° exchange between filled or empty cation orbitals; on the contrary, the ferromagnetic coupling can be formed by 180° exchange between filled and empty cation orbitals or 90° exchange between filled cation orbitals.

Double-exchange Compared to superexchange, which is based on a virtual hopping mechanism, the double-exchange is a real hopping process of electrons among ions with different valence. In other words, the electrons in superexchange are localized, but they are delocalized in double-exchange interaction. Double-exchange often happens between ions in different oxidation states. Furthermore, the electron hopping process is accompanied by the ferromagnetic alignment of the metal atoms.

Interaction in Fe_3O_4 As shown in fig.2.2, there are three dominating interactions:

1. Antiferromagnetic coupling between the T_d and O_h cations, induced by the superexchange interaction with an angle in between of 125° as shown in fig.2.2a.
2. Ferromagnetic coupling between cations on the O_h sites, induced by superexchange interaction with an angle of 92.3° between $\text{Fe}^{2+} - \text{O} - \text{Fe}^{3+}$ as shown in fig.2.2b.
3. Ferromagnetic coupling between cations on the O_h sites, driven by double-exchange interaction as shown in fig.2.2c.

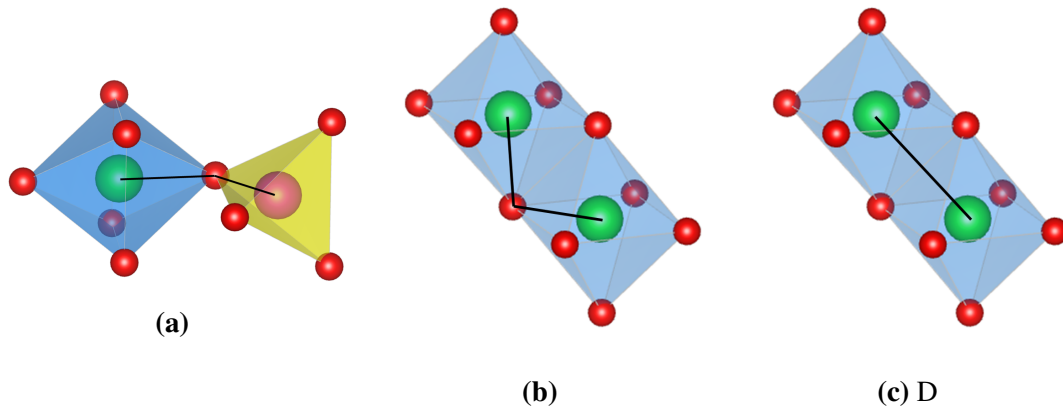


Figure 2.2: The different interactions in the inverse spinel structure drawn by VESTA: (a) the antiferromagnetic superexchange interaction, (b) the ferromagnetic superexchange interaction, and (c) the ferromagnetic double-exchange interaction

Net magnetic spin in Fe_3O_4 As there is antiferromagnetic coupling between the Fe^{3+} on T_d and O_h site, which is the superexchange interaction, the spin of Fe^{3+} in O_h and T_d can compensate each other. As a result, the net magnetic moment is only caused by Fe^{2+} , and is equal to $4\mu_B/\text{f.u.}$

Verwey transition

The Verwey transition is a first-order metal-insulator transition unique to magnetite. It occurs around 120 K [14]. With warming through the Verwey transition temperature (T_V), the magnetite crystal lattice changes from a monoclinic structure to a cubic inverse spinel structure. Conducting behavior of the crystal changes from insulating to metallic.

Magnetocrystalline anisotropy is an intrinsic property of Fe_3O_4 , independent of grain size and shape. Depending on the different orientations of the sample, the magnetization reaches saturation in different fields. It turns out that one would need a lower or higher magnetic field to reach the saturation magnetization depending on the orientation of the field and the crystal. The easy axis is defined as the direction inside a crystal, along which small applied magnetic field is sufficient to reach the saturation magnetization. Conversely, along the hard axis, a larger applied magnetic field is needed. For magnetite above the Verwey transition temperature, $\langle 111 \rangle$ is the easy axis direction of magnetization and $\langle 100 \rangle$ is the hard direction of magnetization. Thus, the magnetization will be saturated in the $\langle 111 \rangle$ direction. However, when the temperature is lower than Verwey transition temperature, with the changing crystal structure, the easy axis

changes to $\langle 100 \rangle$ direction. Magnetocrystalline anisotropy is the energy needed to deflect the magnetic moment in a single crystal from the easy to the hard axis direction.

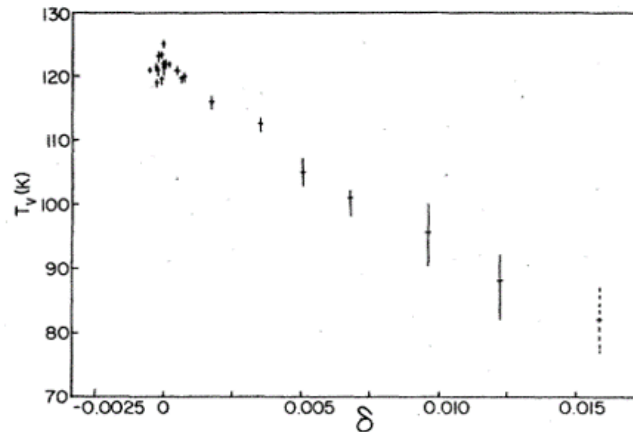


Figure 2.3: Verwey temperature for different oxygen content (figure taken from [1])

The change of crystal structure induces changes in electrical and other physical properties. The first observed change is the metal-insulator transition: when $T > 120\text{K}$, electrons can hop from Fe^{2+} to Fe^{3+} and causes conductivity; when $T < 120\text{K}$, the electron hopping freezes out and the resistivity increases enormously. The Verwey transition is an important property of Fe_3O_4 . Some research has studied the dependence of the Verwey transition on oxygen content [15]. With increasing oxygen content, Fe_3O_4 changes from a first-order phase transition to a second-order transition, and the discontinuity will finally disappear. As shown in fig.2.3, for $\text{Fe}_{3-\sigma}\text{O}_4$, with increasing nonstoichiometric σ , the Verwey transition temperature decreases [1]. Thus, it is a sensitive indicator of stoichiometry.

2.1.2 Wüstite (Fe_{1-x}O)

The reduced iron oxide phase of Fe_3O_4 is wüstite. "Ideal" wüstite is stoichiometric FeO in the rock salt structure which is not a stable phase [16]. As shown in fig.2.1, it has a cubic unit cell with the lattice constant of 4.3\AA and all Fe^{2+} cations occupy the octahedral sites. However, the wüstite samples synthesized below 10 GPa are all deficient in iron, and thus can be represented by the formula Fe_{1-x}O , where $0.04 < x < 0.12$ [17]. This deviation from stoichiometry results from vacancies on Fe^{2+} cation sites, and some of the tetrahedral sites are occupied by Fe^{3+} cations [18][19]. At room temperature Fe_{1-x}O is an antiferromagnetic insulator.

Iron oxide	Color	Crystal structure	Lattice constant (Å)	Magnetic properties	Electric properties
Fe_{1-x}O	Black	Rock salt	4.3	Antiferro	Insulator(RT)
Fe_3O_4	Red	Inverse spinel	8.394	Ferri	Half metal
$\gamma\text{-Fe}_2\text{O}_3$	Red	Defected spinel	8.4053	Ferri	Insulator
$\alpha\text{-Fe}_2\text{O}_3$	Red	Corundum	5.0355	Antiferro	Insulator

Table 2.1: Structure, magnetic and electric properties of iron oxide phases

2.1.3 Maghemite ($\gamma\text{-Fe}_2\text{O}_3$)

The oxidized phase Fe_2O_3 has different phases: α -, γ -, β - and ϵ - Fe_2O_3 . Both β - and ϵ - Fe_2O_3 are metastable. Which means that the Gibbs free energy of this phase is not the smallest under the same composition, temperature and pressure, which drives the phase change to other stable phases[20]. $\gamma\text{-Fe}_2\text{O}_3$ is also a transition state to $\alpha\text{-Fe}_2\text{O}_3$ but with similar properties to Fe_3O_4 . Maghemite ($\gamma\text{-Fe}_2\text{O}_3$) has the same spinel structure as magnetite with a lattice constant of 8.4053\AA and is also ferrimagnetic [21]. Unlike Fe_3O_4 , in the unit cell of maghemite, Fe^{3+} cations occupy both of the tetrahedral and octahedral sites. Additionally, the Fe^{3+} cations are not evenly distributed on the O_h and T_d sites, and thus the magnetization of Fe^{3+} contributes to the net moment ($M_S=2-2.5\mu_B/\text{f.u.}$). Because of the lack of Fe^{2+} , the electrons cannot hop between the different valencies of iron cations [22].

2.1.4 Hematite ($\alpha\text{-Fe}_2\text{O}_3$)

Hematite $\alpha\text{-Fe}_2\text{O}_3$ is the thermodynamically stable phase in the iron oxide family - up to a temperature of 1457°C [23]. The unit cell of $\alpha\text{-Fe}_2\text{O}_3$ has a corundum structure that belongs to the $R\bar{3}c$ space group [24]. The crystal structure can be visualized as alternating iron and oxygen layers stacked along the [001] axis. The iron layers order antiferromagnetically below the Néel temperature. Around $T_M \approx 260\text{K}$, hematite goes through a first-order spin-reorientation transition which is known as the Morin transition. Below $T_M \approx 260\text{K}$ hematite is antiferromagnetic and between $T_M \approx 260\text{K}$ and $T_N \approx 960\text{K}$ it is a weak ferromagnet[25]. Hematite has low conductivity and poor structural stability, thus it is considered an insulator [26].

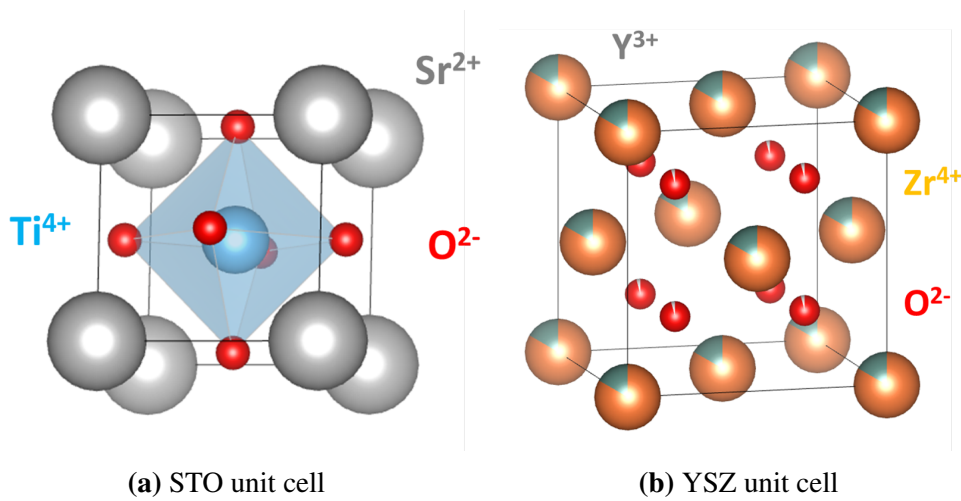


Figure 2.4: The unit cell of different substrate: (a) STO and (b) YSZ

2.2 Oxide substrate: SrTiO_3

The deposition of Fe_3O_4 on oxide substrates can influence the strain state and the oxygen content of the thin films. In this study, we optimize and study the influence of different growth parameters. After characterizing the properties of Fe_3O_4 thin films, we experiment with tuning the iron oxide phase by controlling the oxygen migration between substrates and thin films. Different substrates have different oxygen supply characters. For example, yttria-stabilized zirconia (YSZ) has "inert" oxygen supplying properties. Strontium titanate, on the other hand, can oxidize Fe_3O_4 and supply oxygen to the thin films allowing the control of oxygen migration; the details will be further introduced in section 2.2.3 [6]. Thus, STO is chosen as the substrate to study how to tune the properties of iron oxide. This study is the follow-up to the primary optimization introduced in my project thesis "Optimization of the growth conditions of magnetite films on YSZ substrates".

2.2.1 SrTiO_3 crystal structure

At room temperature, SrTiO_3 has the ABO_3 cubic perovskite structure (space group $\text{Pm}\bar{3}\text{m}$) with a lattice parameter of 3.905\AA . The crystal structure is sketched in fig.2.4a. The Sr^{2+} cations are located in the eight corners of the cubic unit cell and the Ti^{4+} cations are sixfold coordinated by O^{2-} anions[27].

SrTiO₃ is an insulator with a bandgap of 3.2 eV [28]. The electrical conductivity of SrTiO₃ can be changed by the oxygen vacancy doping or by impurity doping (e.g. Nb) [29]. As we aim at controlling the iron oxide phase by applying a voltage; which will be further introduced in section 5, we chose the conducting Nb-doped SrTiO₃ (Nb: STO) as substrate.

2.2.2 Epitaxial growth of Fe₃O₄ on STO substrates

The lattice constants of Fe₃O₄ and STO are 8.395 Å and 3.905 Å, respectively. The unit cell of Fe₃O₄ is slightly bigger than two of the unit cells of STO. The lattice mismatch between Fe₃O₄ (100) and STO (100) is -7.5% as shown in formula 2.1.

$$Mismatch = \frac{2a_{STO} - a_{Fe_3O_4}}{2a_{STO}} = \frac{2 \cdot 3.905 - 8.395}{2 \cdot 3.905} \approx -7.5\% \quad (2.1)$$

This relatively high mismatch makes epitaxial growth difficult. In order to obtain good quality thin films with single crystalline, we optimized the laser fluence with the Fe₃O₄/YSZ system in my project thesis. After this optimization, we get a better quality of Fe₃O₄ thin films also on Nb: STO substrates when grown with the same parameters.

Antiphase boundaries (APBs)

However, the mismatch can still lead to defects during deposition, such as dislocations and antiphase boundaries (APBs) [30]. The anti-phase boundaries originate from the growth mode during deposition. There are islands formed firstly during deposition. The neighboring islands can shift respectively, resulting in the APBs [31]. The APBs are known to influence the structure and properties of Fe₃O₄ thin films [32].

2.2.3 Gibbs free energy

Different oxide substrates can influence the reduction and oxidation at the interface between Fe₃O₄ and substrates [33]. The direction of reduction and oxidation reaction can be determined by the Gibbs free energy. From the thermodynamic definition, a reduction in Gibbs free energy is necessary for a reaction to be spontaneous at constant pressure and temperature. This means when the Gibbs free energy of the oxide substrate

Materials	ΔG^0 (kJ/mol)
Fe ₃ O ₄	-1164.21
YSZ	-1200
SrTiO ₃	-1500
TiO ₂ -terminated STO	-900 to -1039

Table 2.2: Gibbs free energy of the iron oxide and the oxide substrates calculated from the database at room temperature based on the data from [6]

is similar to that of Fe₃O₄, the redox reaction will be not spontaneous. For example, the Gibbs free energy of YSZ ($\Delta G_{YSZ}^0 = -1200$ kJ/mol) is similar to Fe₃O₄, making it ideal to be used for the optimization of growth temperature. However, as shown in table 2.2, the Gibbs free energy of STO is -1500 kJ/mol which is lower than Fe₃O₄ ($\Delta G_{Fe_3O_4}^0 = -1164.21$ kJ/mol). The STO substrate can spontaneously reduce Fe₃O₄ thin film, but also allows control of the oxygen migration [6]. This is the main reason that STO is chosen to be the substrate in our study.

Chapter 3

Experimental methods

This study is focused on the preparation, characterization and tuning of Fe_3O_4 thin films on Nb:STO. The experimental techniques we used will be introduced in this chapter.

3.1 Pulsed laser deposition (PLD)

Pulsed laser deposition (PLD) is a physical vapor deposition (PVD) technique that is widely used to deposit thin films on substrates. In a vacuum chamber, a high-power pulsed laser beam is focused on a Fe_2O_3 target, and therefore, the target material is vaporized in a manner generally referred to as ablation.

The vaporized target material deposits as a thin film on the substrates. This deposition occurs in the presence of a background gas— in our case, oxygen, which is commonly used when depositing oxides to fully oxygenate the deposited films. The deposition parameters influence the quality of the crystallization of thin films.

The PLD process has the following parameters: a 50W KrF excimer laser with a pulse width of 25ns and a wavelength of $\lambda=248\text{nm}$ is used. As shown in fig.3.1, the high-power laser pulse is focused in a vacuum chamber on the rotating target. The material of the target (here Fe_2O_3) is vaporized to form a plasma plume. The ablated material consists of the neutral and ionized species, and then this material is directed to a substrate, which is 50 mm away from the target. The laser fluence F , which is calculated by the energy of laser pulses and the size of the laser spot on the target, is important

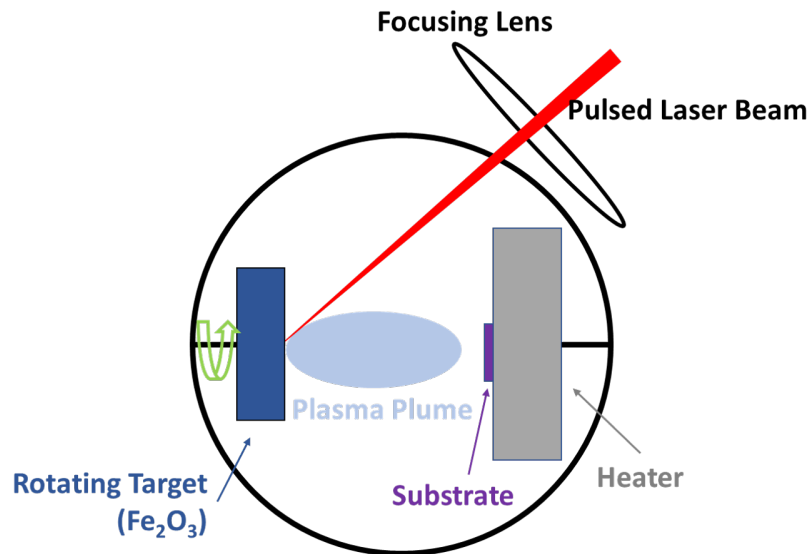


Figure 3.1: Sketch of PLD process

for the ablation process. The laser fluence and the pulse repetition rate can be adjusted between $F = 1\text{-}3 \text{ J/cm}^2$ and $f = 1\text{-}50 \text{ Hz}$, respectively.

The film does not necessarily have the same composition as the target. In order to deposit Fe_3O_4 thin films, we choose the stable phase Fe_2O_3 as the target material. By changing the background oxygen pressure, the desired film stoichiometry can be reached. In this study, the base oxygen pressure is $1 \times 10^{-7} \text{ mbar}$. In addition, the substrate is mounted on a heater which can reach a maximum of 850°C . By controlling the heater temperature, sufficient energy can be introduced for adatoms to diffuse and arrange themselves to form the desired crystalline structure.

3.2 Atomic force microscopy (AFM)

The Atomic Force Microscope Agilent 5400 is used here to characterize the surface morphology of the films and substrates with a sub-nanometer resolution. By measuring the interaction force between the tip and the sample, an image of the topography of a sample surface at a high resolution can be easily made.

As shown in fig.3.2, the laser is reflected by the cantilever to the detector. Tapping mode is the most common mode of AFM. In tapping mode, the cantilever is driven to oscillate

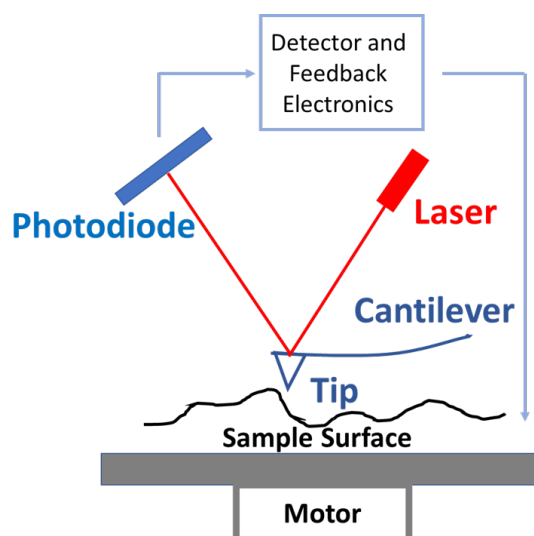


Figure 3.2: Principle of AFM measurement

near its resonant frequency, which is achieved with a piezo element in the cantilever holder. The frequency and amplitude of the driven signal are kept constant. When the tip is close enough to the sample surface, interaction forces affect the amplitude of cantilever oscillation. Through a feedback system, the height of the cantilever is adjusted, and thus the surface topography is mapped.

3.3 X-Ray Reflectometry/ Diffractometry (XRR and XRD)

X-Ray Reflectometry is a sensitive tool to characterize the surface of a thin film, here two devices are used: Bruker D8 Advance from JCNS-2 and Bruker D8 Advance from PGI-7 (thanks to Prof. Dittmann). They share the same principle but have different resolutions and options. A Cu-source is used as an X-ray source with a wavelength $\lambda=1.54\text{\AA}$ in both instruments.

As shown in fig.3.3, the X-Ray goes through slits and is reflected by a smooth sample to the detector. By analyzing the intensity of the reflected X-Rays, we can get information on the thickness and roughness of the thin film.

At the surface of thin film samples, both reflection and refraction of X-Ray occur as

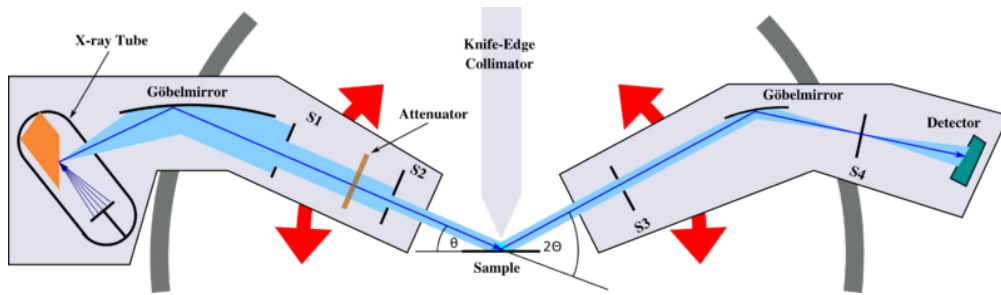


Figure 3.3: Sketch of D8 XRR (figure taken from ref. [2])

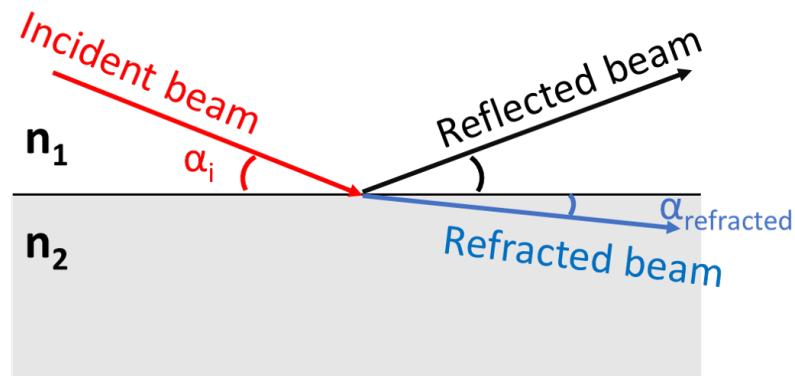


Figure 3.4: Reflection and refraction of X-ray

shown in fig.3.4. The relation between incident and refracted X-Ray beam is:

$$n_1 \cos(\alpha_i) = n_2 \cos(\alpha_{refracted}) \quad (3.1)$$

The index of refraction of most materials is smaller than one, the index of refraction of air is equal to one. As a result, when we consider an X-Ray beam incident from the air and refracted in a thin film, then there would be a critical angle α_c for the incident beam. When the incident angle α_i is smaller than α_c there is no refraction, which is called “total internal reflection”. For a Fe_3O_4 thin film, $\alpha_c = 0.2^\circ$.

For a single thin film system, the refracted beam will be reflected at the interface between the substrate and thin film, then constructive interference occurs with the reflected beam at the surface of the thin film, as shown in fig.3.6. This phenomenon causes the oscillation pattern called “Kiessig fringes”. By analyzing the period of these oscillations, thin film layer thickness and interlayer roughness can be calculated. X-ray reflectivity measurements are often analyzed by fitting the measured data to a simulated curve. Fitting parameters are layer thickness, densities, roughness. Here, the program GenX [38]

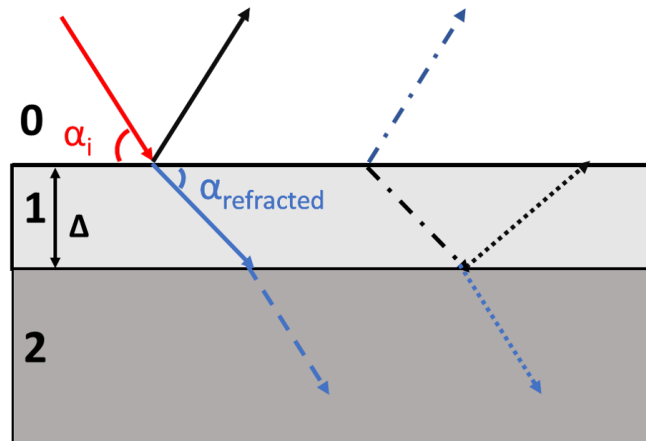


Figure 3.5: Constructive interference in a single thin film system

is used for analysis.

An X-Ray diffractometry experiment is also an ideal tool to characterize the crystal structure of thin film layers. Based on Bragg's law (formula 3.2), incident X-ray shows an interference pattern after interaction with the crystal lattice. The lattice constant d is easily calculated:

$$2d\sin\theta = n\lambda \quad (3.2)$$

λ : the wavelength of X-ray which is 1.54\AA in our device

n : A whole number

This can be used to calculate the out-of-plane lattice constants of the crystal in order to study the strain and stress state inside the thin film system.

3.4 Vibrating sample magnetometer (VSM)

The PPMS DynaCool from Quantum Design is used here [3]. In the DynaCool, a single two-stage Pulse Tube cooler is used to cool the system, providing a continuous low-temperature control (1.9K to 400K) and precise field (magnetic field up to $\pm 9\text{T}$) and temperature sweep modes.

By using vibrating sample magnetometer (VSM) mode, the influence of the environment can be minimized and the magnetic properties of samples measured. First, a sample is magnetized in a uniform magnetic field and then sinusoidally vibrated. The

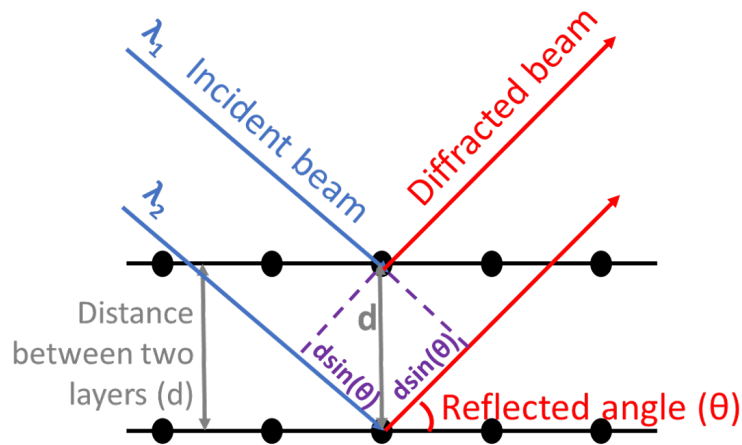


Figure 3.6: Bragg's law

magnetic field is generated by a superconducting solenoid which has a vertical field, meaning it aligns with the $\langle 100 \rangle$ axis of the sample.

By using VSM, the magnetic moment of the substrate and thin film can both be measured. By subtraction of the diamagnetic part of the substrate, the magnetic moment of the Fe_3O_4 thin film can be extracted.

3.5 Magnetic properties measurement system (MPMS)

The magnetic properties measurement system (MPMS) from Quantum Design is used for characterizing magnetization properties (Data taken from Magnetic Property Measurement System MPMS MultiVu Application User's Manual). It uses a Superconducting QUantum Interference Device (SQUID) to measure the net magnetization of samples in the temperature range $T = 2 - 400\text{K}$ and the field range $B = -7 - +7\text{T}$. The resolution is ca. $1 \times 10^{-7} \text{emu}$. The sample is mounted on a plastic straw and then held by the socket head and inserted into the MPMS chamber which is filled with helium. The magnetic moment of the sample induces a current in the coils and is then coupled into the SQUID circuit. This current is measured to calculate the magnetic flux. Thus, the SQUID system can reach a sensitivity of $5 \times 10^{-12} \text{Am}^2$.

To apply a voltage on the sample and to measure magneto-electric coupling, a sample holder of the standard (DC) transport option is used. The magneto-electric setup was



Figure 3.7: VSM coil set and linear transporter (figure taken from ref. [3])

implemented by Dr. O.Petracic (JCNS-2) in order to apply a voltage. As shown in fig.3.8, the sample is contacted with two copper wires. The two ends of each copper wire are removed to get rid of the insulation part using a scalpel blade. Then, using silver paint, the wires are connected to the surface of the thin film and the bottom of the substrate, respectively. As Fe_3O_4 thin films and Nb: STO substrates are both conducting material, the silver paint is applied in as small a drop as possible. After the sample is contacted properly, it is inserted into the straw with the contact wires coming out at both ends of the straw. The wires are then wrapped to the screws on the holder. The connecting of different screws of the holders and the different sides of samples are kept the same during the experiment in order to apply the voltage always with the same



Figure 3.8: Sample connected with SQUID holder by copper wire

polarity.

A reciprocating sample option (RSO) is normally used for the movement of the sample. RSO uses a servo to rapidly oscillate the sample and results in a higher sensitivity. However, the electrical connection is not possible for the RSO option. Thus, the DC option has to be used in our measurement.

3.6 Wide-Angle X-ray Scattering (WAXS)

Based on Bragg's equation, wide-angle x-ray scattering (WAXS) is an x-ray scattering characterization method. It is installed on the Gallium anode low-angle x-ray instrument (GALAXI) platform [4]. GALAXI can investigate structures in the order of 2 - 100 nm. Unlike small-angle x-ray scattering (SAXS), the distance from the sample to the detector for WAXS is shorter, and a wider range of angles is observed. Thus, WAXS is better for investigating crystalline material with long range order. A sketch of the GALAXI platform is shown in fig. 3.9.

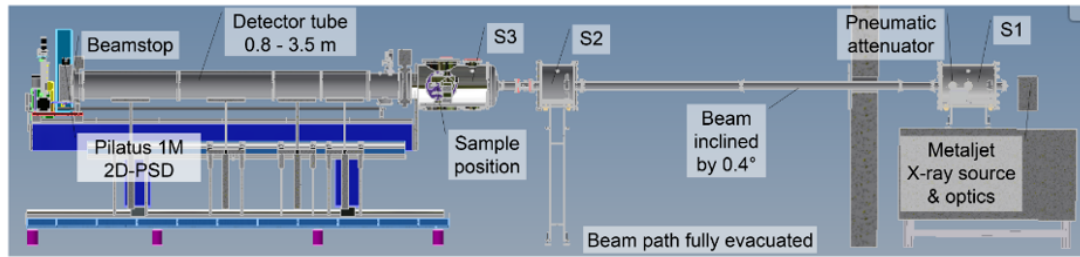


Figure 3.9: Sketch of GALAXI platform (figure taken from [4])

GALAXI uses the Bruker AXS Metal jet X-ray source in Chamber S1 in fig.3.9. An electron beam of $20\mu\text{m}$ height \times $80\mu\text{m}$ width at 70 keV energy and 200 W power hits the liquid metal jet and X-rays are produced. The optics allow only the Ga K_{α} to pass and produce a monochromatic X-ray with the wavelength of 1.3414\AA . The sample is mounted on a rotator in Chamber S3 which allows the sample to rotate horizontally with changing ω . The wide-angle detector is installed in the S3 chamber. As shown in fig.3.10, the detector is placed at a certain distance (D) from the sample, for WAXS, this distance is around 85mm ($D \approx 85\text{mm}$). Furthermore, the detector is placed at a certain angle to the sample, this angle is decided with regard to the peaks of interest. Of note: changing the angle of the detector can only be done manually, which brings systematic error into the calculations. The detector is from DECTRIS, the length of the detector is 64mm with 1280 pixels on it. For a certain angle of the sample, the incident beam is diffracted into a region which will be collected by all the pixels of the detector with different 2θ . By rotating the sample, we can get a series of $\omega - 2\theta$ data which allows us to look into reciprocal space.

3.7 Reciprocal space mapping (RSM)

By plotting the data in a reciprocal space map, we can extract information from the X-ray diffraction pattern in detail. This detail can include the deviation from perfect crystal structure which allows us to understand the different in-plane and out-of-plane strain state which can influence the physical properties of thin film materials. The vector $\underline{r^*(hkl)}$ from the origin to the reciprocal lattice point (h,k,l) is normal to the (hkl) plane of the crystal lattice. Every point in reciprocal space represents a possible reflection from the crystal lattice. Moreover, the length of the vector $\underline{r^*(hkl)}$ is the reciprocal of the spacing of the (hkl) planes in real space. Thus, the nth point from the origin in a given row in the reciprocal lattice corresponds to the nth order reflection from the (hkl)

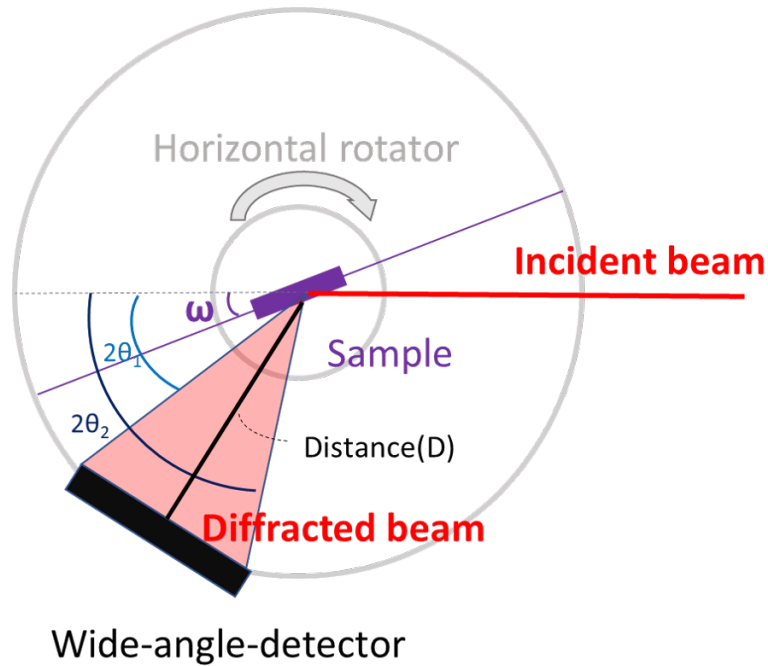


Figure 3.10: Sketch of the diffraction process in WAXS

crystal planes.

Not all the points in reciprocal space correspond to a reflection, but they should also fulfill Bragg's equation. This phenomenon is described by Ewald's sphere. As shown in fig.3.11, the incident wave and diffracted wave are given by \underline{k}_i and \underline{k}_f , respectively. For the case of elastic scattering, both vectors have the same length which is reciprocal to the wavelength: $|\underline{k}_i| = |\underline{k}_f| = 1/\lambda$. The scattering vector \underline{Q} is given by the difference between two vectors as shown in equation 3.3.

$$\begin{aligned}\underline{Q} &= \underline{k}_f - \underline{k}_i \\ |\underline{Q}| &= 2\sin\theta/\lambda\end{aligned}\quad (3.3)$$

With $|\underline{Q}| = |\underline{d}_{hkl}^*| = 1/d_{hkl}$, we can fulfill Bragg's equation:

$$\begin{aligned}|\underline{Q}| &= 2\sin\theta/\lambda = 1/d_{hkl} \\ \lambda &= 2d_{hkl}\sin\theta\end{aligned}\quad (3.4)$$

The diffraction happens in a different direction of \underline{k}_f when its endpoint lies at a reciprocal lattice point hkl . All possible \underline{k}_f describe a sphere with a radius of $2\pi/\lambda$, which is

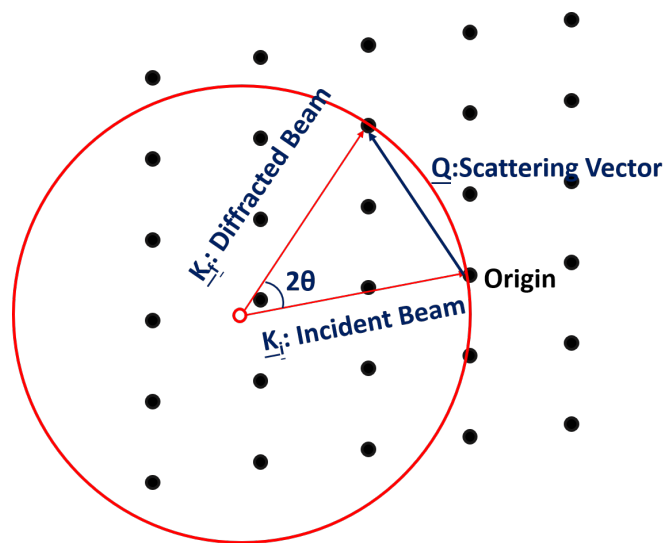


Figure 3.11: Illustration of diffraction using Ewald's sphere

Ewald's sphere.

Chapter 4

Growth optimization of $\text{Fe}_3\text{O}_4/\text{STO}$

4.1 Substrate preparation

The 10mmx10mmx0.5mm Nb: STO substrates from Crystec GmbH are first etched in HF for 1min by our colleague Sylvia de Waal from PGI-7 . Two kinds of termination exist on the surface of STO: TiO_2 -termination and SrO termination. As mentioned in section 2.2 TiO_2 -terminated STO can supply oxygen into thin films. The HF etch removes Sr more efficiently than Ti. Thus, STO substrates can be etched in HF at room temperature to obtain a TiO_2 -terminated structure [25]. The etching procedure reduces the surface roughness by removing Sr from the Nb: STO substrate surface and produces a step-and-terrace surface structure. However, the substrate surface after etching is not stable. However, by annealing at over 800°C the structure of the etched surface is stabilized. In our experiment Nb: STO substrates are annealed at 950°C for 2.5 hours with a ramp of 1.5 hours after etching [34] [35]. In fig.4.1 the AFM images of the (a)original substrate, (b) after etched in HF for 1min and (c) after annealing at 950°C for 2h are shown. After treatment of etching and annealing, the surface with the terraced structure is obtained with the step width of $0.905 \mu\text{m}$.

4.2 AFM

Because of the large mismatch between Fe_3O_4 thin film and Nb: STO substrates, the epitaxial deposition is challenging. The growth temperature is important for the crystal

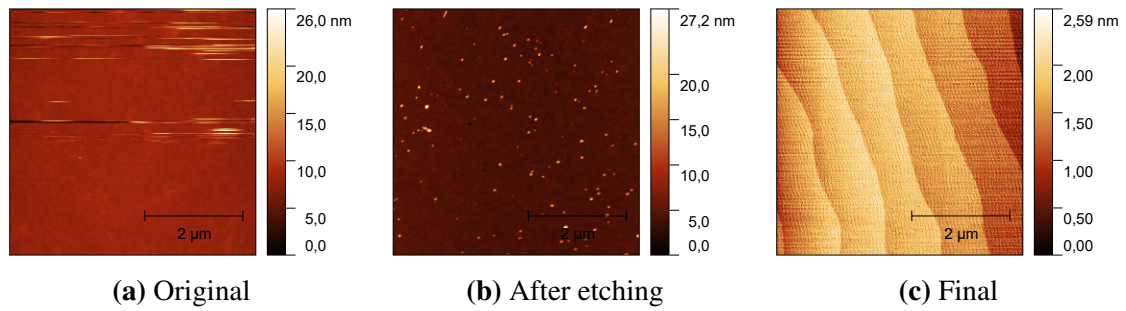


Figure 4.1: Treatment to Nb: STO substrate: (a) original substrate, (b) substrate after etching in HF for 1min and (c) substrate after etching and then annealed at 950°C for 2 h

structure of the Fe_3O_4 thin film, which will influence the physical properties of the film. The surface morphology, roughness, and thickness can be characterized by atomic force microscopy (AFM) and X-ray reflectivity (XRR).

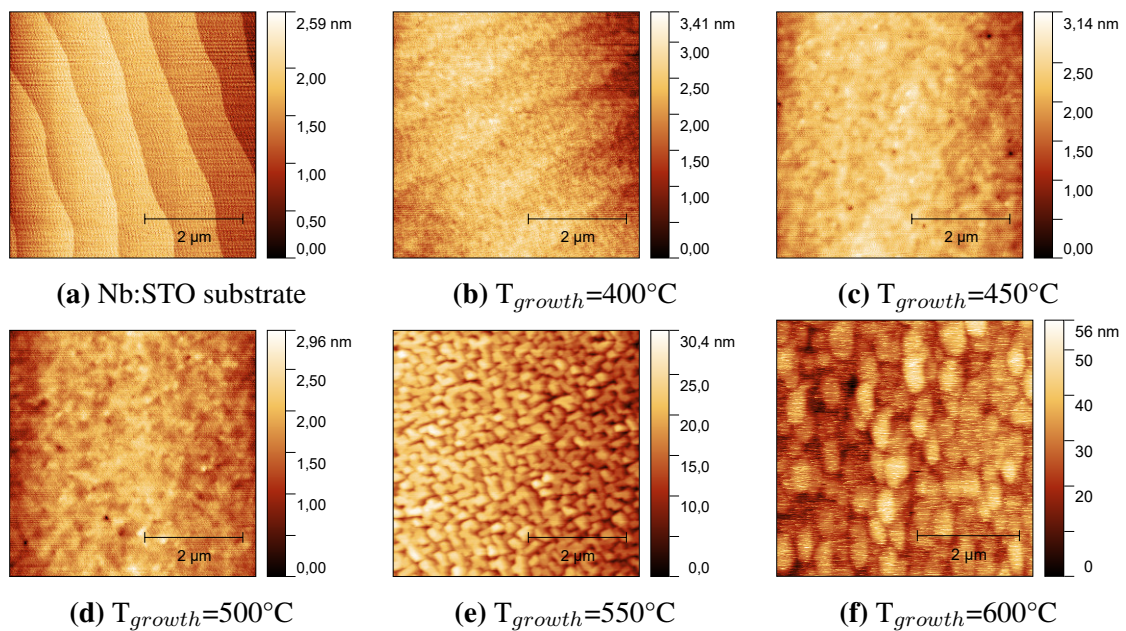


Figure 4.2: $5 \times 5 \mu\text{m}$ AFM images of (a) Nb: STO substrate and Fe_3O_4 thin films grown on Nb: STO substrates at the growth temperature of (b) 400°C, (c) 450°C, (d) 500°C, (e) 550°C and (f) 600°C

The AFM measurements are done in tapping mode in the air by Atomic Force Microscope Agilent 5400. The scan size is a square of $5 \mu\text{m} \times 5 \mu\text{m}$. AFM $5 \mu\text{m} \times 5 \mu\text{m}$ 2D scans of Fe_3O_4 films grown at different temperature of $T_{\text{growth}}=400, 450, 500, 550,$

600°C are displayed in Fig. 4.2. Comparing the etched Nb: STO substrate as shown in Fig. 4.2(a), the Fe₃O₄ films grown at 400°C keep the terraced structure of the substrate. For the Fe₃O₄ films grown at 450 and 500°C the underlying terraced structure becomes indistinct. For the Fe₃O₄ films grown over 500°C, Fig.4.2e and 4.2f show the absence of step structure of the Nb: STO substrates. Thus we deduce that during the deposition the thin film doesn't adopt the structure of the substrate's surface. Instead of growing layer by layer, the undesired island growth is formed during growth on the substrates. The surface roughness can be furthermore analyzed by Root Mean Square (σ_{RMS}), analysis in the Gwyddion software[36]. The surface roughness is 0.13, 0.40, 0.51, 3.56, 8.91 nm for the thin films grown at 400, 450, 500, 550, 600°C, respectively. The roughness increases strongly with increasing growth temperature, also indicating the loss of layer-by-layer structure during growth. Thus, when $T_{growth}=400, 450, 500^\circ\text{C}$, we can make good quality of Fe₃O₄ thin films on Nb: STO substrates with small roughness.

4.3 XRR

X-ray reflectivity (XRR) is used to investigate the surface roughness and thickness of the thin film by using Bruker D8 Advance.

For incident angles below the critical angle ($2\theta < 0.4^\circ$), we have total internal reflection. Above the critical angle, the roughness of the thin films causes exponential intensity decay of the reflected wave. Thus, the intensity drops faster with increasing roughness. Besides the roughness of the thin film surface, the thickness can also be determined. Interference occurs between X-ray reflected from the surface of the thin films and the refracted part of X-ray reflected from the interface. This interference causes oscillations of reflectivity intensity. These oscillations were first witnessed by Kiessing in 1931 and are thus named Kiessing fringes [37]. The film thickness can be calculated from the period of the oscillations. The thicker the film is, the shorter the period of oscillation.

Fig.4.3a shows the X-ray reflectivity of Fe₃O₄ thin films at different growth temperatures in the range of $2\theta=0.1^\circ-5^\circ$. The sample grown at 550 and 600°C shows a much faster drop after the critical angle compared to the others, which indicates a higher roughness, consistent with the AFM measurements. The measured reflectivity intensity data is fitted by GenX[38]. The thickness and roughness are calculated after the fitting.

The thickness of all thin films grown under different temperatures are all around 40 nm with a deposition time of 25 min. The roughness of the films obtained by fitting is shown in fig. 4.3b. Although generally the roughness is much higher than the results

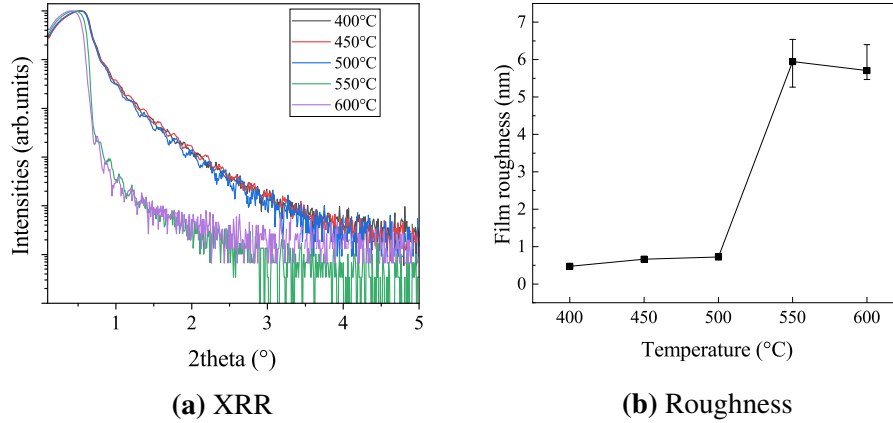


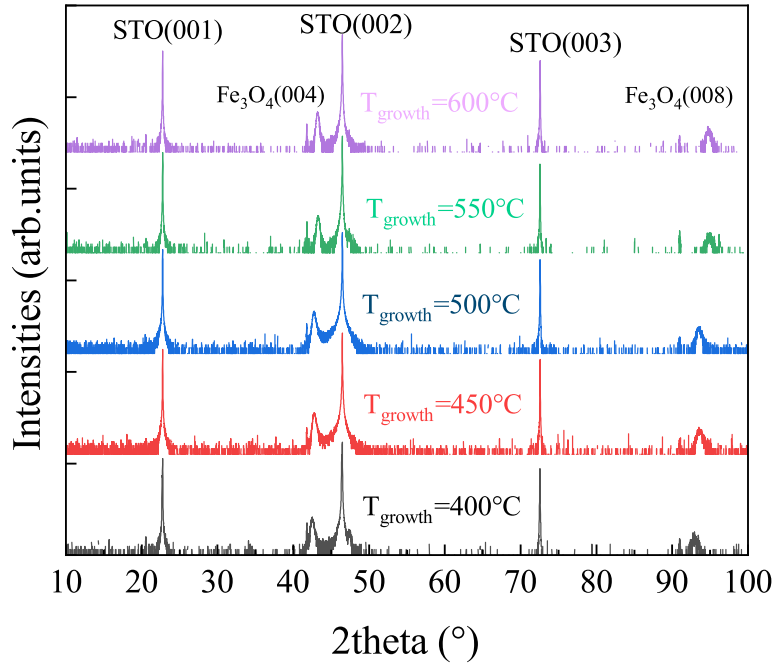
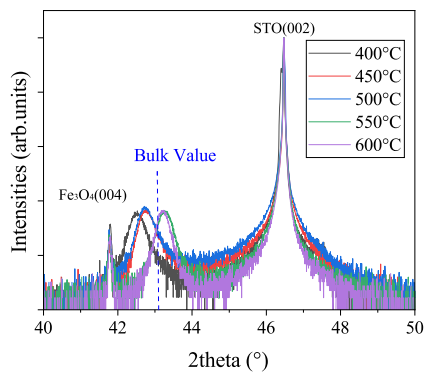
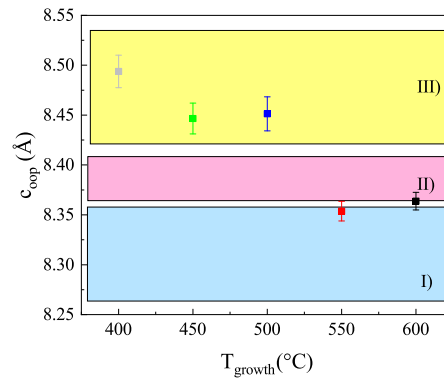
Figure 4.3: (a) X-ray reflectivity of samples grown at different temperatures, (b) surface roughness of films calculated from XRR

obtained in AFM, it shows a similar trend. The thin films grown at 550 and 600°C show a much higher roughness than the others which corresponds to the results from AFM. This increasing roughness correlates with the high growth temperature. When the temperature is too high, energy is supplied for an atom to diffuse and form the island-like structure which contributes to the roughness.

All in all, by analyzing AFM and XRR results, we found the thin films have good quality when the growth temperature is under 550°C.

4.4 XRD

After checking the bulk film quality with AFM and XRR results, we use X-ray diffraction (XRD) to analyze the out-of-plane crystallinity of the thin films by using the Bruker-D8. Fig. 4.4a shows the XRD scan of $\text{Fe}_3\text{O}_4/\text{Nb: STO}$ system with the 2θ range from 10° to 100° . The results are normalized to the STO (002) reflection. The substrate peaks, STO (002) and STO (004) reflection, are strong and clear, which helps to align the beam. The sharp peak around 40° is caused by Cu K_β . Using the formula 3.2, the 2θ value of STO (002) is associated not only with the lattice constant but also the wavelength of the X-ray source. For Cu K_α , the wavelength is 1.54\AA , which causes the strongest peak of STO(002) around 46.4° , while the wavelength of Cu K_β is 1.39\AA and causes the peak around 40.1° . In between, the two peaks of Fe_3O_4 in (004) and (008) direction all appear, while the other characteristic peaks of Fe_3O_4 do not. This indicates

(a) XRD between $2\theta=10^\circ-100^\circ$ (b) XRD between $2\theta=40^\circ-50^\circ$ 

(c) Out-of-plane lattice constant

Figure 4.4: Out-of-plane X-ray diffraction scans of Fe_3O_4 thin films grown at different temperatures of (a) all reflection in the range of $2\theta=10^\circ-100^\circ$ and (b) Fe_3O_4 (004) reflection in the range of $2\theta=40^\circ-50^\circ$. (c) the out-of-plane lattice constant c_{opp} with different force regions: I) tensile strain, II) relaxed growth and III) compressive strain.

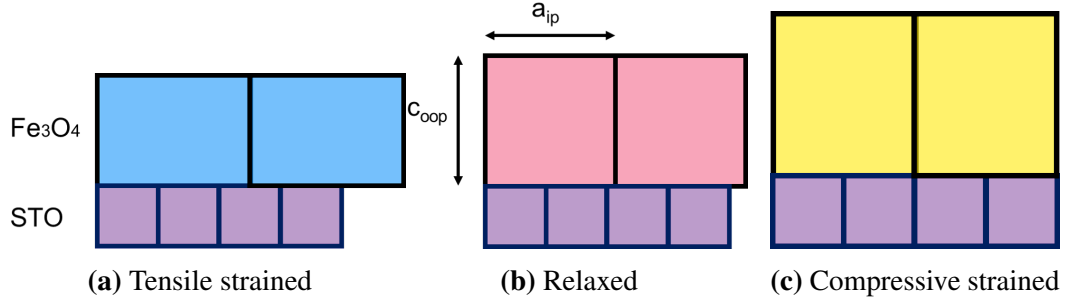


Figure 4.5: Sketches of Fe_3O_4 crystal unit cells on STO in different situations: I) tensile strained, II) relaxed and III) compressive strained.

the Fe_3O_4 crystals grow in the same direction in the out-of-plane direction. In other words, films at all temperatures are grown $(001)_{\text{Fe}_3\text{O}_4} \parallel (001)_{\text{STO}}$.

In order to investigate the local behavior, fig.4.4b shows the XRD scan with the 2θ ranged from 40° to 50° around the STO (002) and Fe_3O_4 (004) reflection. The bulk value of the Fe_3O_4 (004) peak is around $2\theta=43.1^\circ$ (blue dashed line). For all the Fe_3O_4 films grown at different temperatures, the Fe_3O_4 (004) peak positions are slightly shifted. The (004) peak occurs at a smaller angle when $T_{\text{growth}} = 400^\circ\text{C}$, 450°C and 500°C , while the same peak occurs at a larger angle when $T_{\text{growth}} = 550^\circ\text{C}$ and 600°C .

As mentioned in section 2.1.1, the bulk lattice constant of Fe_3O_4 crystal in (100) direction at room temperature is 8.395\AA , and it is 3.911\AA for STO in (100) direction. Approximately two lattices of Fe_3O_4 fit in one of the STO units. The mismatch is -7.5% which makes the epitaxial growth of Fe_3O_4 difficult to achieve and causes strain in the Fe_3O_4 films. Ideally, as shown in fig.4.5b the Fe_3O_4 film grows relaxed which means the out-of-plane lattice constant (c_{oop}) and the in-plane lattice constant (a_{ip}) should be equal to the bulk value 8.395\AA ($c_{\text{oop}} = a_{\text{ip}} = 8.395\text{\AA}$). In contrast, as shown in fig. 4.5c, if the film is completely compressively strained, then the in-plane lattice constant of Fe_3O_4 films should be equal to two times the in-plane lattice constant of the substrate ($a_{\text{substrate}}$), which means $a_{\text{ip}} = 2 a_{\text{substrate}} = 7.822\text{\AA}$. If we assume the volume of the unit cell remains constant, then the out-of-plane lattice constant will become larger with the decreasing in-plane lattice constant for the films. Vice versa, as shown in fig. 4.5a when with tensile strain, the out-of-plane lattice constant will become smaller with increasing in-plane lattice constant. By using Bragg's law given in formula 3.2, the out-of-plane lattice constant can be calculated corresponding to the XRD 2θ value. It is plotted in fig. 4.4c with changing growth temperature. The region of plots can be divided into three parts, I) tensile strain, II) relaxed growth and III) compressive strain.. Generally, the out-of-plane lattice constants of Fe_3O_4 films grown under all temperatures from 400°C

to 600°C are all near to the bulk value of 8.395Å. For $T_{growth} = 400^\circ\text{C}$, 450°C, and 500°C, c_{oop} is larger than the bulk value, which means the thin films are grown with compressive strain. However, when $T_{growth} = 550^\circ\text{C}$ and 600°C, c_{oop} is slightly smaller than the bulk value, indicating the thin film's lattice is almost relaxed.

4.5 WAXS

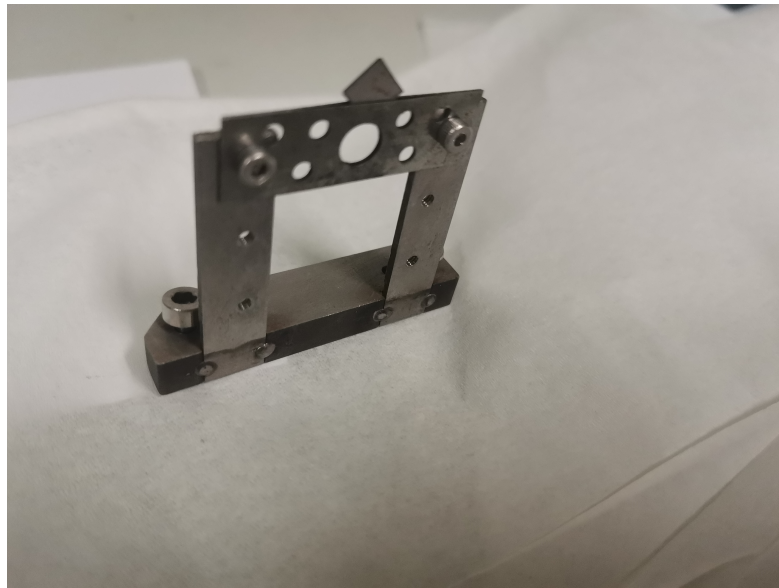


Figure 4.6: The mounting of samples in the WAXS holder

As XRD can only observe the reflection peak in the out-of-plane direction, we turn to WAXS to investigate the in-plane and out-of-plane structure change. As introduced in section 3.6, the detector can collect data with different 2θ which is realized by 1280 Pixels. The sample is mounted on the holder and rotated with it. Samples mounted in different directions can show different reflections. In our experiment, we want to measure the (hhl) reflection of the sample, thus, we mount the sample with 45° rotation as shown in fig. 4.6.

Then we can investigate the reflection intensities with different ω and 2θ values. The data can be converted from real space $2\theta - \omega$ to the reciprocal space $Q_x - Q_z$ or $a_{ip} - c_{oop}$ with different units. The details about the calculation of the data from WAXS are introduced in Appendix A.

The reflection of every peak can be identified by plotting them in the reciprocal space

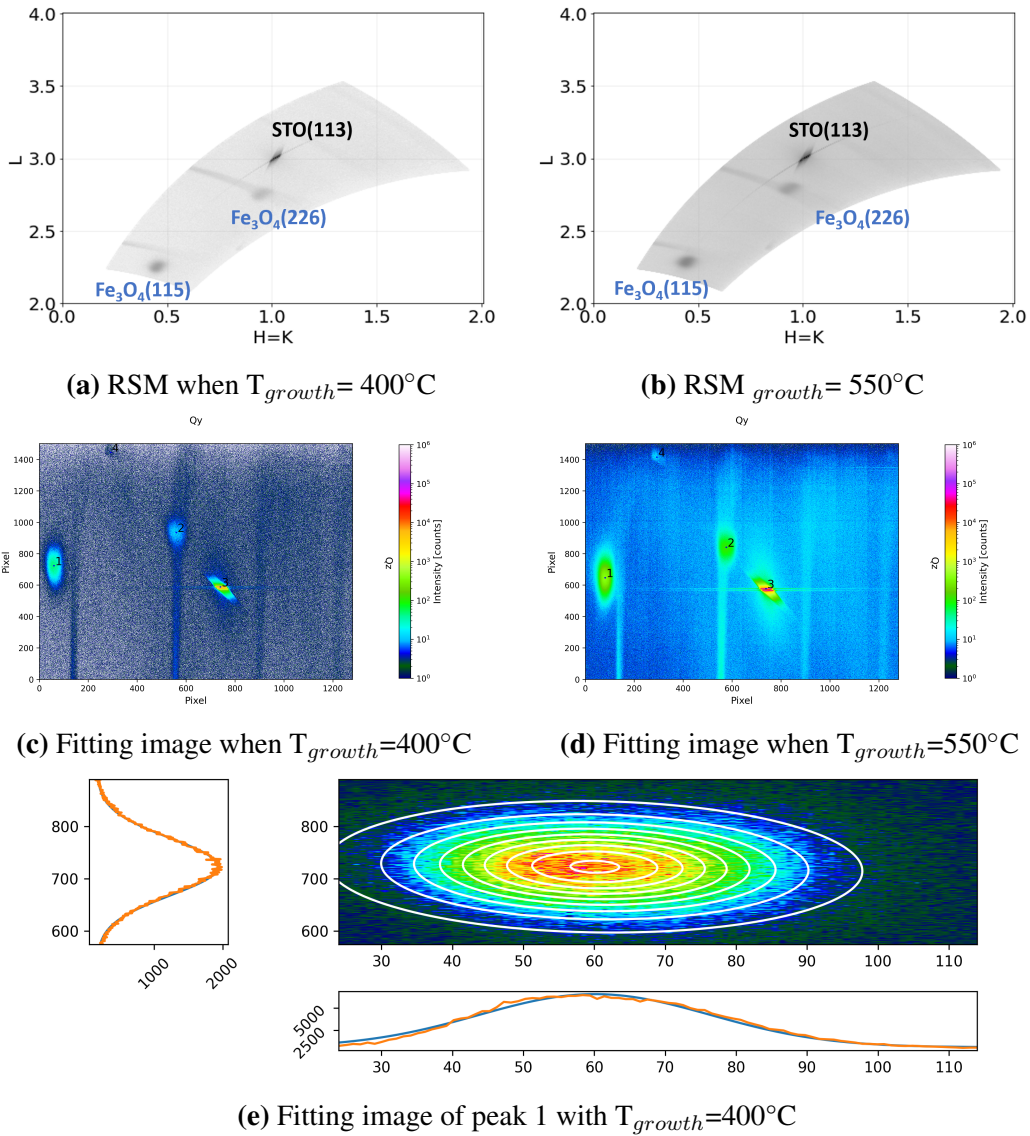


Figure 4.7: Peak fitting and RSM for samples grown at 400 and 550°C

with the STO unit or Fe₃O₄ unit. Fig. 4.7a and 4.7b represents the reciprocal space in STO unit of Fe₃O₄ thin films on Nb: STO substrates with $T_{growth} = 400$ and 550°C , respectively. By comparing fig. 4.7a and 4.7b, we observe a shift of Fe₃O₄ peaks, indicating the different strain states. However, the peaks of Fe₃O₄ are relatively broad and weak (the intensities are almost 1/10000 of the substrate peak). As introduced in Appendix B, the in-plane and out-of-plane can be calculated from the known (hkl) and the Q_x , Q_z value. As we need accurate 2θ and ω value to calculate Q_x and Q_z , as shown in fig. 4.7c and 4.7e, we use the peak finder program, which is developed by

Paul Zakalek (JCNS-2), to abstract the accurate peak position and the error. Then we can calculate the a_{ip} and c_{oop} with respect to different peaks.

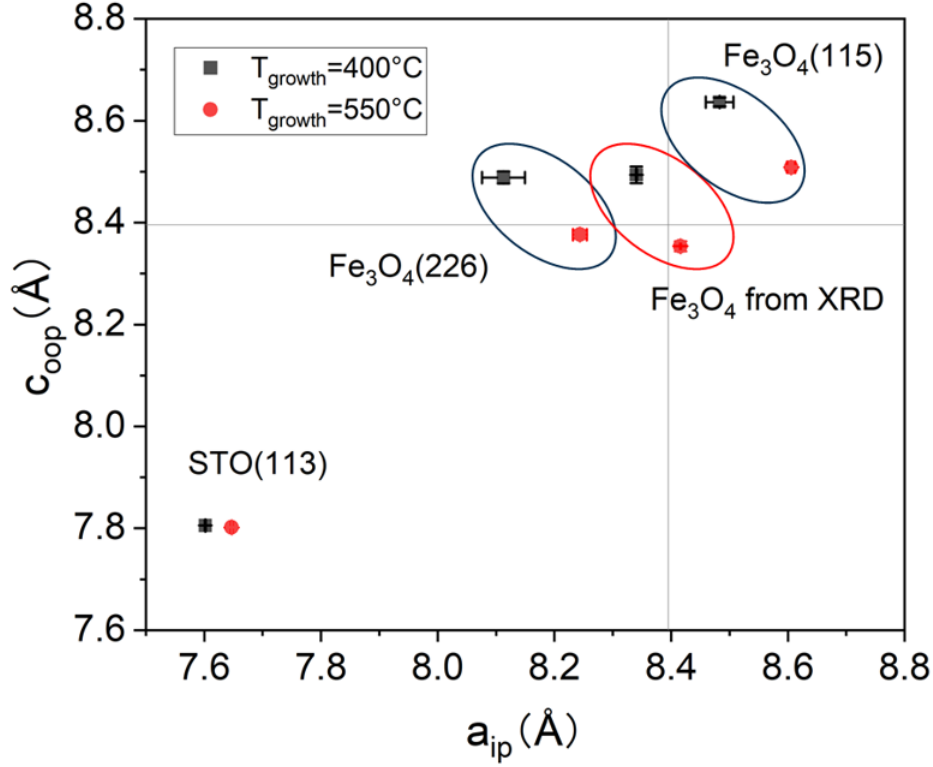


Figure 4.8: In-plane and out-of-plane lattice constant calculated from WAXS and XRD

As shown in fig.4.8, the a_{ip} and c_{oop} of different peaks of samples with different growth temperatures are plotted. Among it, the lattice constant of the substrate is multiplied by 2 as one of the Fe_3O_4 unit cells will fit double of the STO unit cell. As mentioned in fig. 4.4c, the c_{oop} is calculated from the 2θ of Fe_3O_4 . When we assume the volume of the unit cell is a constant, we can calculate the a_{ip} with the equation:

$$a_{ip} = \sqrt{8.395^3 / c_{oop}}$$

The lattice constant of STO should be the same. However, we observed the different lattice constants calculated from STO(113) reflection of the samples with $T_{growth}=400$ and 550°C . The reason for this difference is systematic error introduced by the WAXS experimental set-up, particularly between different sample measurements. As introduced in Appendix B, there are several possible systematic error sources introduced in the

WAXS system which need to be addressed. These errors also account for the difference in the lattice constants of the same growth temperature calculated from different film peaks.

However, although WAXS cannot currently offer an accurate number, it still can give us a blueprint of the possible tendency. Compared to the difference of the lattice constants of $T_{growth}=400$ and 550°C calculated from STO(113) reflection, the lattice constants calculated from Fe_3O_4 show more apparent difference. They all follow the same tendency: the sample grown at 400°C has a smaller a_{ip} and correspondingly a bigger c_{oop} . This consistency indicates that the sample grown at 400°C has a smaller a_{ip} which is more near to double the STO unit cell. The reason for the change of the lattice constant is the epitaxial growth mode. The film would tend to adopt the lattice constant of the substrates and be strained at the interface and then relaxed in the bulk of the film as introduced in fig.4.5

4.6 VSM

The vibrating sample magnetometry (VSM) of device PPMS DynaCool (Quantum Design) is used to characterize the magnetic properties of samples. Magnetization versus temperature ($M(T)$) curves are recorded in zero-field cooling (ZFC) and field-cooling (FC) mode with an applied field of $H=500$ Oe in the direction of STO and Fe_3O_4 $\langle 100 \rangle$ -axis (in-plane). The magnetization versus field hysteresis loops ($M(H)$) are also recorded at different temperatures $T=10$ - 300K in the range of $H=\pm 2\text{T}$.

4.6.1 Saturation magnetization

As mentioned in section 2.1.1, due to the crystal structure of Fe_3O_4 , the spins of Fe^{3+} in O_h and T_d can compensate each other. As a result, the net magnetic moment is only caused by the Fe^{2+} cations, which is $4\mu_B/\text{f.u.}$. In other words, the theoretical value of magnetite thin films should be $4\mu_B/\text{f.u.}$. In order to study the saturation magnetization of our samples, $M(H)$ behavior has been measured. The hysteresis $M(H)$ loops are measured by VSM by applying a magnetic field parallel to the in-plane axis $\langle 100 \rangle$ of the thin films. As shown in fig. 4.10, the Fe_3O_4 thin films grown at different temperatures showed rather different magnetization behaviors. The saturation magnetization for different growth temperatures and measured temperatures are all similar and around $3 \mu_B/\text{f.u.}$. As mentioned before the theoretical value should be $4 \mu_B/\text{f.u.}$, the lower satu-

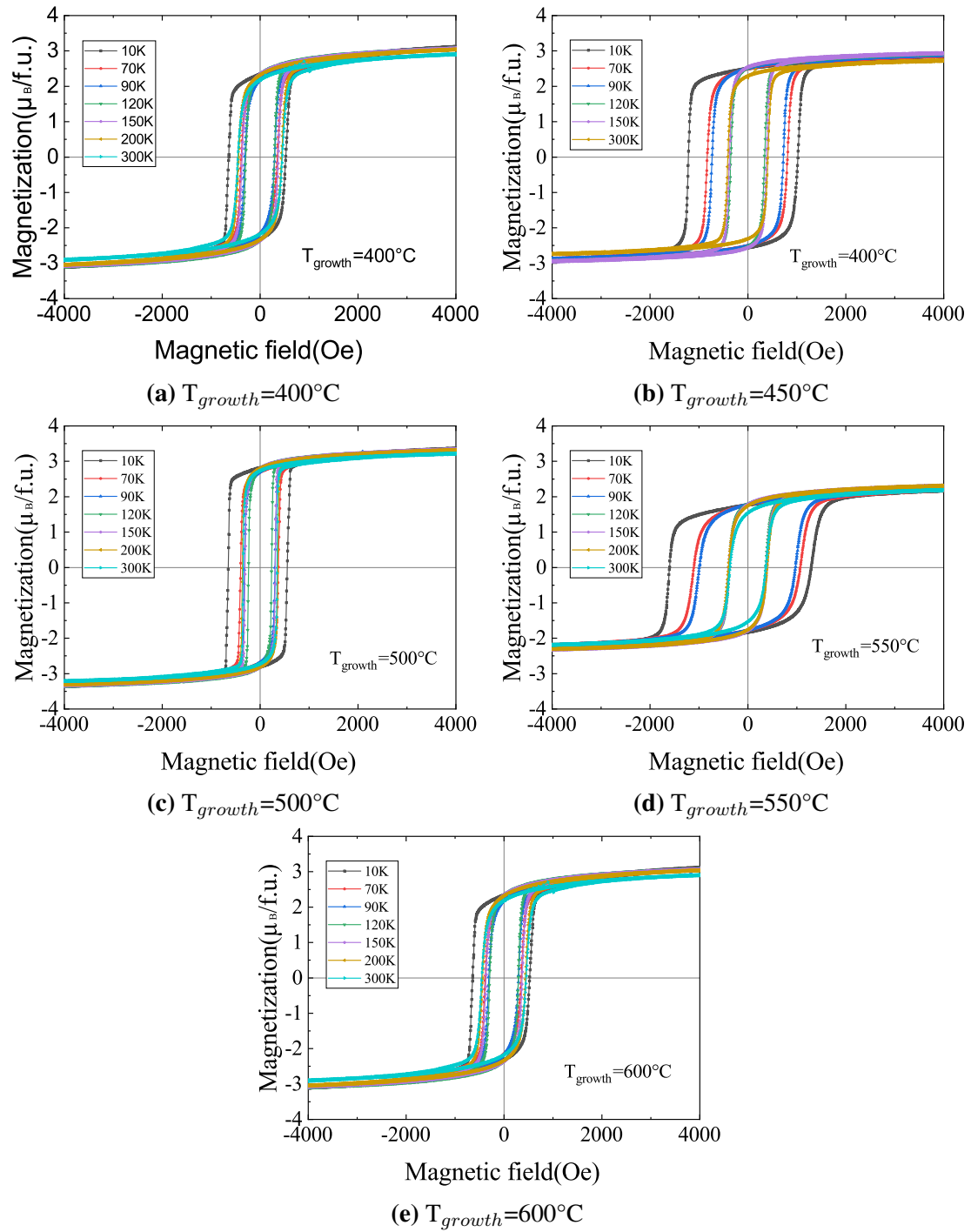


Figure 4.9: Magnetization versus magnetic field Hysteresis for Fe_3O_4 thin films on Nb:STO substrates at the different growth temperature

ration magnetization could originate from the structures while growing. Under different growth temperatures, dislocations and anti-phase boundaries may arise due to the high mismatch of -7.5%. These kinds of anti-phase boundaries are anti-ferromagnetic, which would contribute to the lower saturation magnetization.

4.6.2 Coercivity and remanence magnetization

Different from the saturation magnetization, coercivity field H_C and remanent magnetization M_r are not constant for different temperatures. Magnetic coercivity is the resistance to changes in magnetization. Coercivity is usually referred to as the magnetic field required to demagnetize the material [39]. As for our $\text{Fe}_3\text{O}_4/\text{STO}$ system, magnetite is a ferromagnetic material. Fig. 4.10a shows the coercive field for Fe_3O_4 films grown at different growth temperatures dependent on the measurement temperature. With the different tendencies, we can divide the graph into two regions to study.

When $T > 120\text{K}$, the coercivities of thin films grown at different temperature show slight changes, but all remain between 100 – 500Oe. The coercivity of bulk Fe_3O_4 is around 157Oe. The higher measured coercivity could be due to dislocations and anti-phase boundaries formed during the deposition of thin films. When $T < 120\text{K}$, with decreasing

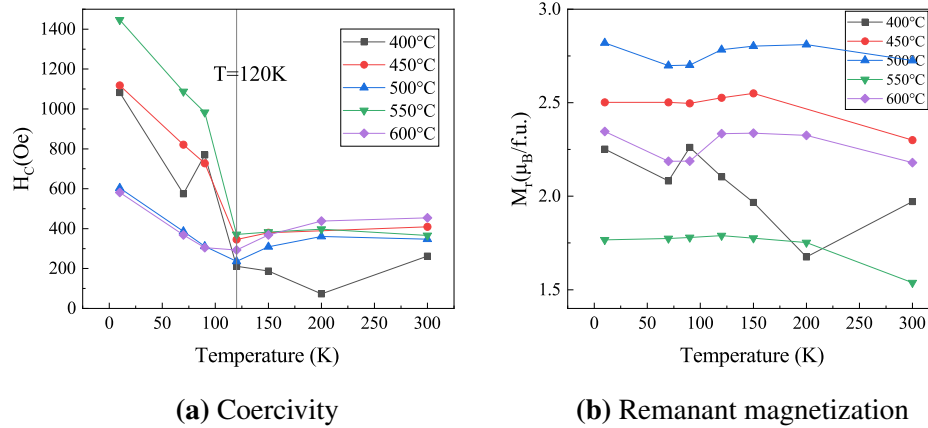


Figure 4.10: (a) Coercive field H_C and (b) remanant magnetization M_r for Fe_3O_4 films grown at different growth temperatures and measured at different temperatures.

temperature, the coercivity increases rapidly. This change is due to the structural transition from cubic to monoclinic through the Verwey transition temperature. Furthermore,

Fe_3O_4 thin films grown at different temperatures show different behavior. The samples grown at lower growth temperature show a stronger increase with the decrease of temperature. This difference could arise from the different strain states with different growth temperatures. Fig. 4.10b shows the change of remnant magnetization for Fe_3O_4 films grown at different growth temperatures with measurement temperature. For most of the growth temperatures, the remnant magnetization is almost constant. Only the sample grown under 400°C shows a difference.

4.6.3 Verwey transition

The Verwey transition temperature reflects the stoichiometry of the Fe_3O_4 thin films. What's more, because of the structural transition around the Verwey transition temperature, magnetization properties are affected. We should detect the first-order transition around 120K when cooling down the system. In order to calculate the specific Verwey transition temperature, we measured the change in magnetization with temperature for samples grown at different growth temperatures shown in fig. 4.11. The magnetization is measured with zero-field cooling and with applying 500 Oe magnetic field. The maximal of first derivation $\frac{dM}{dT}$ can be used to derive the Verwey transition temperature T_V , the transition width ΔT_V can be derived by the distance between max. and min. of the second derivation $\frac{\partial^2 M}{\partial T^2}$.

As shown in Fig. 4.11f, all Verwey transition temperatures are below the bulk value of 124K. With increasing growth temperature, Fe_3O_4 shows a lower Verwey transition temperature and a bigger error range. Verwey transition temperature can be influenced mainly by the oxygen stoichiometry, as reported in Barber's study, for $\text{Fe}_{3(1-\delta)}\text{O}_4$, when $-0.0005 < \delta < \delta_c = 0.0039$, Verwey transition is still a first-order transition. However, when $\delta_c < \delta < 3\delta_c$ it becomes a second-order transition and the discontinuity will disappear [40]. In between, with increasing oxygen content, the Verwey transition temperature will be lower and the width broader. Thus, the general lower trending of the Verwey transition temperature in our experiment could be due to imperfect oxygen stoichiometry. As the Verwey transition temperature is an indicator of the stoichiometry of Fe_3O_4 thin film, we conclude the Fe_3O_4 thin films grown at $T_{\text{growth}} = 400^\circ\text{C}$ and 450°C are either more stoichiometric or more relaxed than the films grown at higher temperatures.

Moreover, as shown in fig. 4.12, the transition width is calculated and shown as the error of Verwey transition temperature. Thus we found with lower growth temperature, Fe_3O_4 thin film have a better oxygen stoichiometry with a more bulk-like Verwey transition temperature and a smaller transition width. In contrast, Fe_3O_4 thin films grown at higher

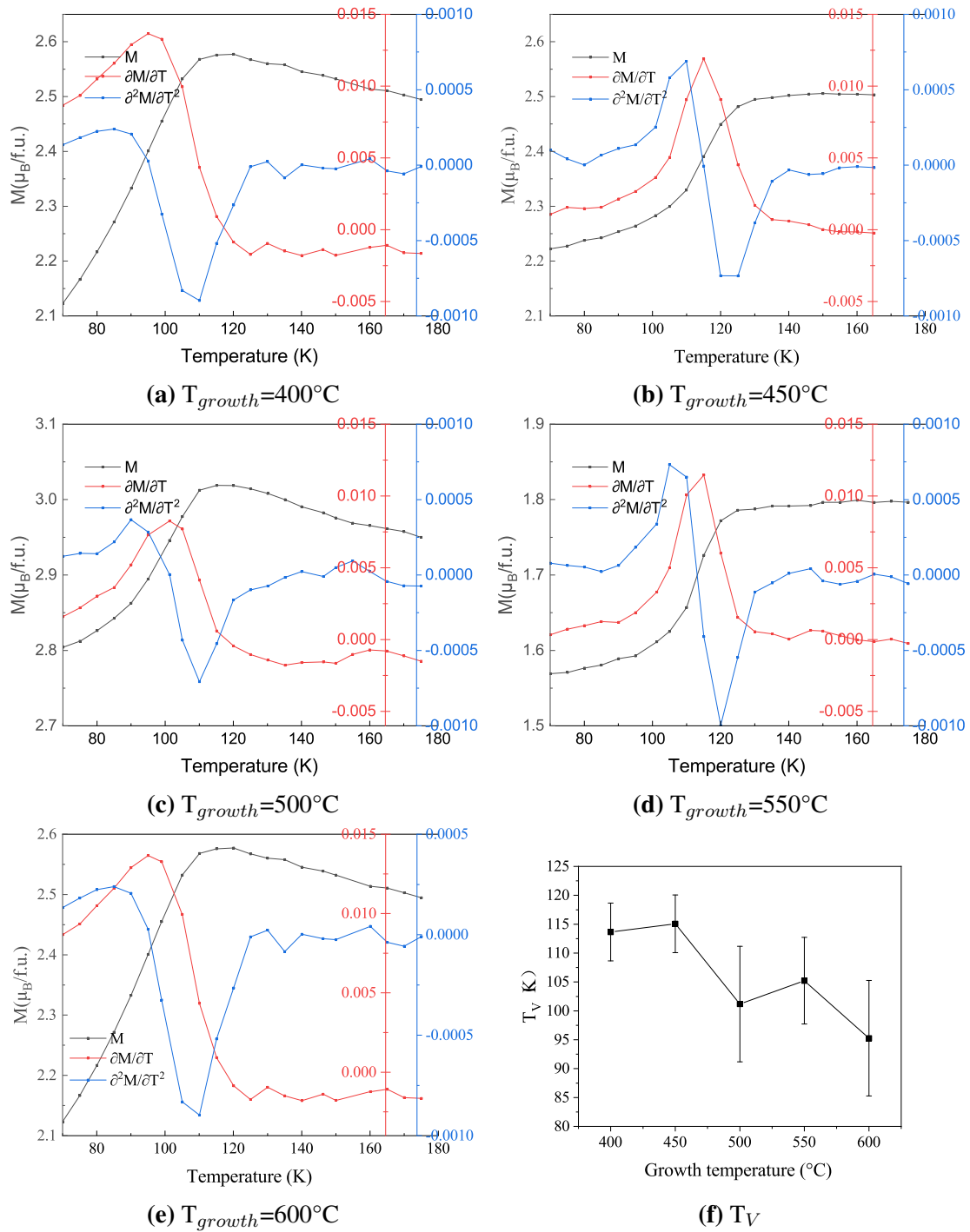


Figure 4.11: (a)-(e): the magnetization versus temperature curves and (f) the Verwey transition temperature calculated from the curves for Fe_3O_4 films grown at different temperature

$T_{\text{growth}}(^{\circ}\text{C})$	$T_V(\text{K})$	Magnetization drop(%)
400	113.6524±5	11.15746
450	115.0666±5	11.22208
500	101.1801±10	7.10571
550	105.21507±7.5	14.54105
600	95.2646±10	17.61738

Figure 4.12: Magnetization properties of Fe_3O_4 thin films grown at different temperatures calculated from M(T) ZFC curve.

temperatures show a more deviate Verwey transition temperature and a larger transition width. Magnetization drop is also calculated and shown in fig. 4.12. All samples show a relatively high magnetization drop. By comparing with the measurements in $\langle 011 \rangle$ in-plane direction in our further study, the easy axis of Fe_3O_4 on STO can be determined.

4.7 Conclusion

In this chapter, we discussed the influence of the growth temperature under certain laser fluency on the different properties of the Fe_3O_4 thin films grown on the SrTiO_3 substrates by pulsed laser deposition (PLD). The morphology of the thin films was investigated by AFM and XRR. We observed the relatively smooth surface with low roughness when growth temperature is under 600°C which indicates a good quality thin film. From the XRD measurements, the structure of the Fe_3O_4 thin films are studied. We observed all peaks of Fe_3O_4 in the same direction which indicates the single crystallinity. In addition, for different growth temperatures, the characteristic Fe_3O_4 (004) peak shows a shift from the bulk value which indicates the different strain state of Fe_3O_4 thin films on STO substrates. With WAXS, we studied the in-plane strain state of Fe_3O_4 thin films. Because of systematic errors in the WAX set-up that still need to be addressed, we cannot get precise quantitative results. However, we observed the same tendency of the lattice constant calculated from different reflections. The in-plane lattice constant of the sample grown at 400°C is more near to the substrate value than at 550°C . This result is also consistent with the lattice constant calculated from the XRD data.

From VSM measurements, two parts of magnetization properties are studied: saturation magnetization and Verwey transition. We observed the saturation magnetization lower than the bulk value because of the assumed presence of anti-phase boundaries. The Ver-

wey transition temperature was calculated from the magnetization versus temperature curve. As a good indicator of oxygen stoichiometry, we find that the samples grown at 400°C and 450°C show the Verwey transition temperature closest to the bulk value and the ones grown higher than 450°C far away. This indicates the different strain states and oxygen stoichiometry among different growth temperatures.

Chapter 5

Tuning the properties of thin films by electric field: in-situ SQUID

5.1 Magnetization tuned by an electric field

We discussed the growth optimization of Fe_3O_4 thin films on STO substrates and observe the different strain states and oxygen stoichiometry for samples under different growth temperatures. In this chapter, we aim to tune the properties of Fe_3O_4 thin films by applying an electric field.

In order to obtain different properties of Fe_3O_4 , we can tune the iron oxide phase. Fe_3O_4 is a half-metal ferrimagnetic material with the net moment of $4\mu_B/unit$ and Fe_2O_3 is a ferrimagnetic insulator with the net moment of $2 - 2.5\mu_B/unit$. Tuning of the iron oxide phase can be achieved by controlling the oxygen migration from the substrate into the film. Nb: STO substrates are etched in HF in order to dissolve the SrO-termination and obtain a TiO_2 -terminated substrate. The oxygen exchange is termination dependent, with TiO_2 -termination, the oxygen vacancy allows the oxygen anions to exchange between thin films and substrates[5].

As mentioned in section 3.5, MPMS SQUID is used to measure the magnetization with applying a vertical voltage. First, we measured the zero field cooling $M(T)$ curve of Fe_3O_4 thin films grown at 600°C as shown in fig.5.1a. The Verwey transition temperature is originally 95.84K without applying an electric field (black curve). By applying $+6\text{V}$ (red curve), the Verwey transition disappears. As mentioned in section 2.1.1, the

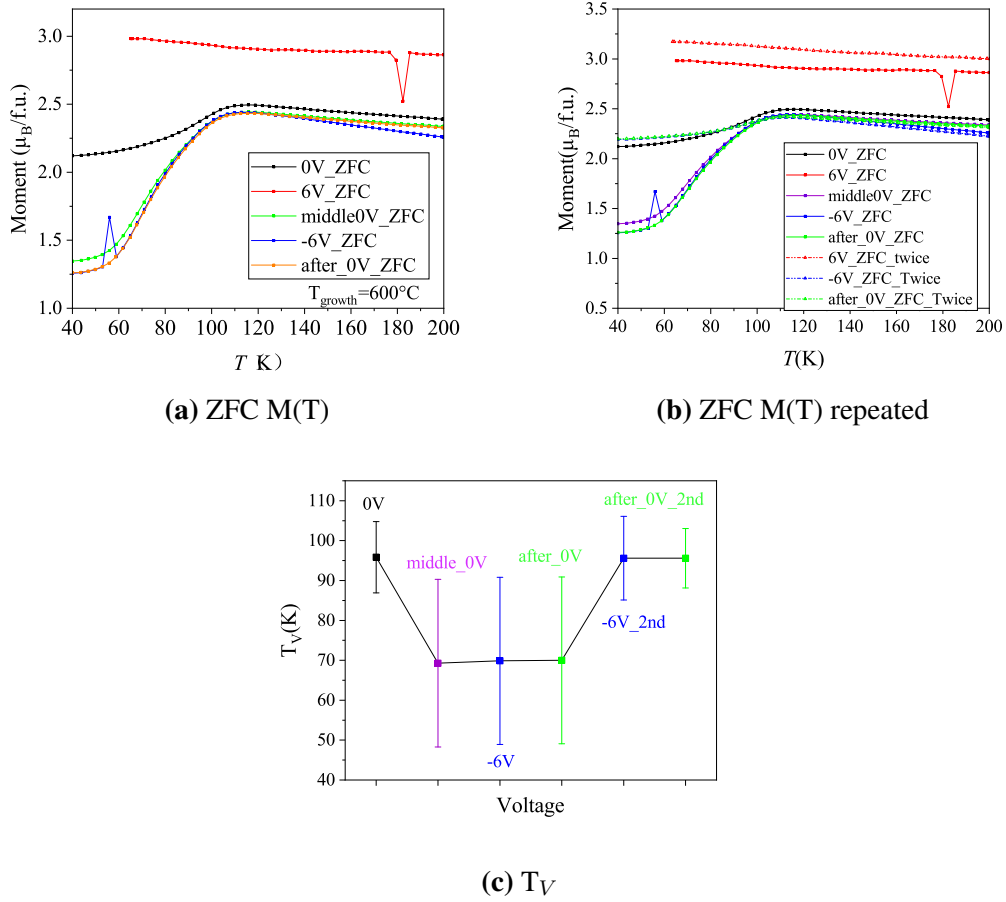


Figure 5.1: ZFC curves (a)original, (b)repeated, and (c) Verwey transition temperature of sample grown under 600°C with applying different voltage

existence of Verwey transition is associated with the oxygen content in the thin film system. With applying a positive voltage, the oxygen anion is driven to migrate through the interface from TiO_2 -terminated STO substrate to Fe_3O_4 thin films as shown in fig. 5.2a. With more and more oxygen anion migrated to the thin film, Fe_3O_4 finally changes to Fe_2O_3 and loses the Verwey transition. Thus, we observed the disappearance of Verwey transition when applying +6V.

Next, we stop the voltage supply and measure ZFC M(T) with again 0V (green curve, middle-0V), the transition appears again but with a lower Verwey transition temperature of 69.30K. The existence of Verwey transition at middle 0V can indicate the oxygen migration is driven by the voltage and when we stop the power supply, the oxygen anion also stops migrating into the thin films and Fe_2O_3 transforms back to Fe_3O_4 but

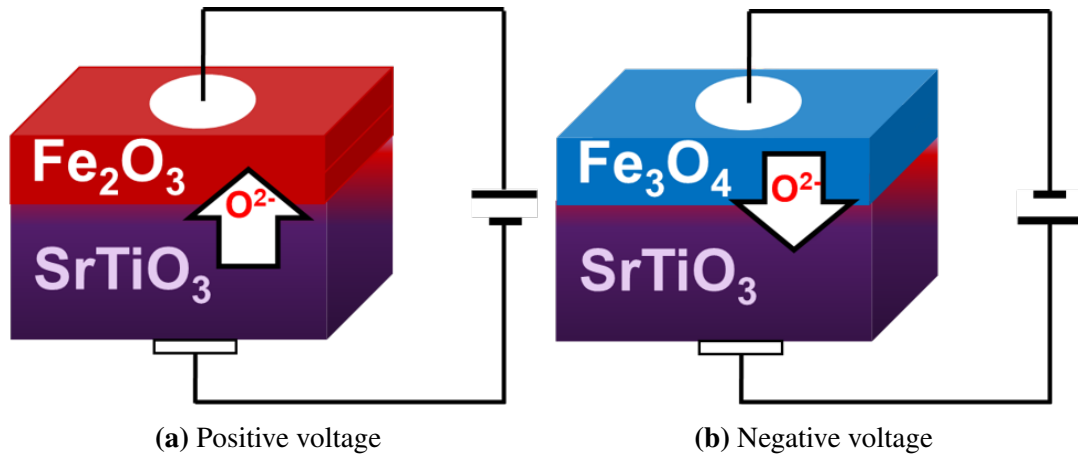


Figure 5.2: The sketch of $\text{Fe}_3\text{O}_4/\text{TiO}_2$ -terminated Nb: STO with applying (a) positive voltage and (b) negative voltage

with poorer oxygen stoichiometry.

When we apply -6V , the Verwey transition temperature stays similar. This procedure is reproducible. Fig. 5.1b shows the repeated ZFC curve of the sample with applying voltage after the first tuning. The behavior under $+6\text{V}$ is the same: both of them lose the Verwey transition, indicating the higher oxygen content and the transition from Fe_3O_4 to Fe_2O_3 .

However, there is a difference between the Verwey transition temperature for -6V and the 0V after -6V . The second time, when we apply -6V , the Verwey transition temperature is 95.60K which is very near to the original 95.84K . The calculated Verwey transition temperature for a different round with different applying voltages are plotted in fig. 5.1c. There are two peaks of the first derivation in 5.3a which could be induced not only by the Verwey transition but also the defects in the $\text{Fe}_3\text{O}_4/\text{Nb:STO}$ system. This defects caused the big difference of the Verwey temperatures calculated from different round.

The absence of Verwey transition under positive voltage shows up for the samples grown at different temperatures. For Fe_3O_4 grown at 450°C and 550°C , we observe the negative magnetization at a low temperature at a certain voltage as shown in fig. 5.4a and 5.4c.

This negative magnetization phenomenon is usual in the SQUID system. The residual fields can be generated by circulating currents in the superconducting filaments [41]. This residual field is a random value inside $[-10, +10]$ Oe. In our system, it stays at -2 Oe for years, measured by Dr. Oleg Petravic. This means, when theoretically we

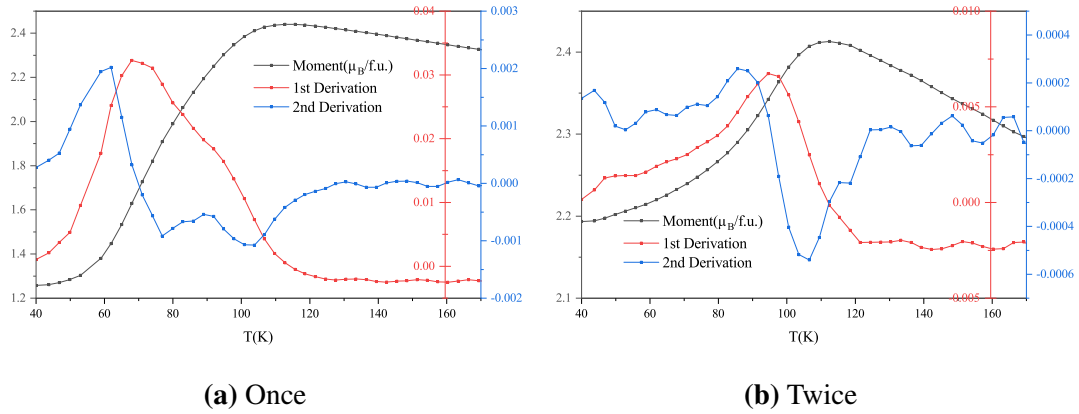


Figure 5.3: ZFC, 1st and 2nd Derivation with applying -6V for (a) the first time and (b) the second time

cool the system to low temperature before ZFC measurement, there is actually a small negative field $H_{RS} \approx -2$ Oe applied, then the samples are cooled with negative magnetization. When we start to warm up the system in the ZFC measurement, we apply a field $H_a = 500$ Oe. The samples have intrinsic coercive field $H_c(T)$ which is changing with the temperature. When in the low temperature, $H_c(T_{low}) < H_a$, the applied field H_a can not reverse the system. Thus, the magnetization stays negative. With increasing measuring temperature, When $H_c(T_{low}) < H_a$, the applied field compensates for the coercivity, the magnetization reverses to be positive. To confirm if this is the problem of this residual field, we need to measure it in the future. After confirmation, we can apply a small field when cooling the system which can compensate for the residual field. If the negative magnetization phenomenon can also be influenced by magnetic anisotropies[42].

5.2 Structure tuned by electric field: ex-situ XRD

As mentioned in section 4.4, the magnetite thin films on Nb: STO substrates only show the single crystallinity along the [004] direction. As shown in fig. 5.5, we did ex-situ XRD after applying the voltage in SQUID to check the crystal structural change compared with the original data. For the samples grown at 450 and 550 °C (fig. 5.5a, 5.5b), there appears a new peak around 37.1° after applying voltage in SQUID. This could be the (222) peaks of Fe_3O_4 or $\gamma\text{-Fe}_2\text{O}_3$. The iron oxide is driven by an electric field to align in different directions or have structural change. This change is not temporary,

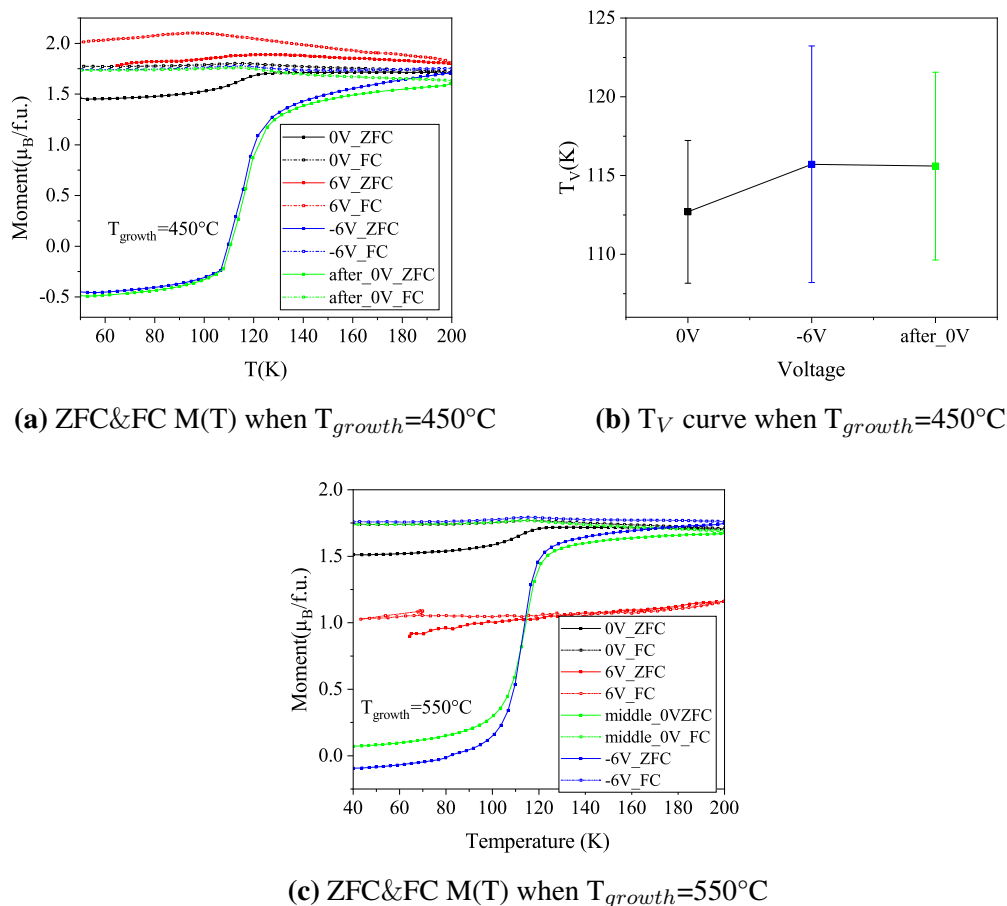


Figure 5.4: (a) ZFC&FC curves and (b) Verwey transition temperature of sample grown under $450^\circ C$ and (c) ZFC&FC curves when $T_{growth}=550^\circ C$ with applying different voltage

thus, we can observe it in ex-situ XRD even after weeks. In fig. 5.5b, the peak of Fe_3O_4 is slightly shifted to the left. This could indicate the formation of $\gamma-Fe_2O_3$. Maghemite has a spinel structure similar to Fe_3O_4 with a larger lattice constant. According to Bragg's equation, the 2θ value should be smaller. However, as the other samples didn't show this slight shift, we need to confirm the iron oxide composition in our future study. As shown in fig. 5.5c, the sample grown at $600^\circ C$ doesn't show the new peak around 37.1° after applying voltage in SQUID. This could be due to the different growth parameters, or different times of applying voltage; which is an interesting topic for future studies.

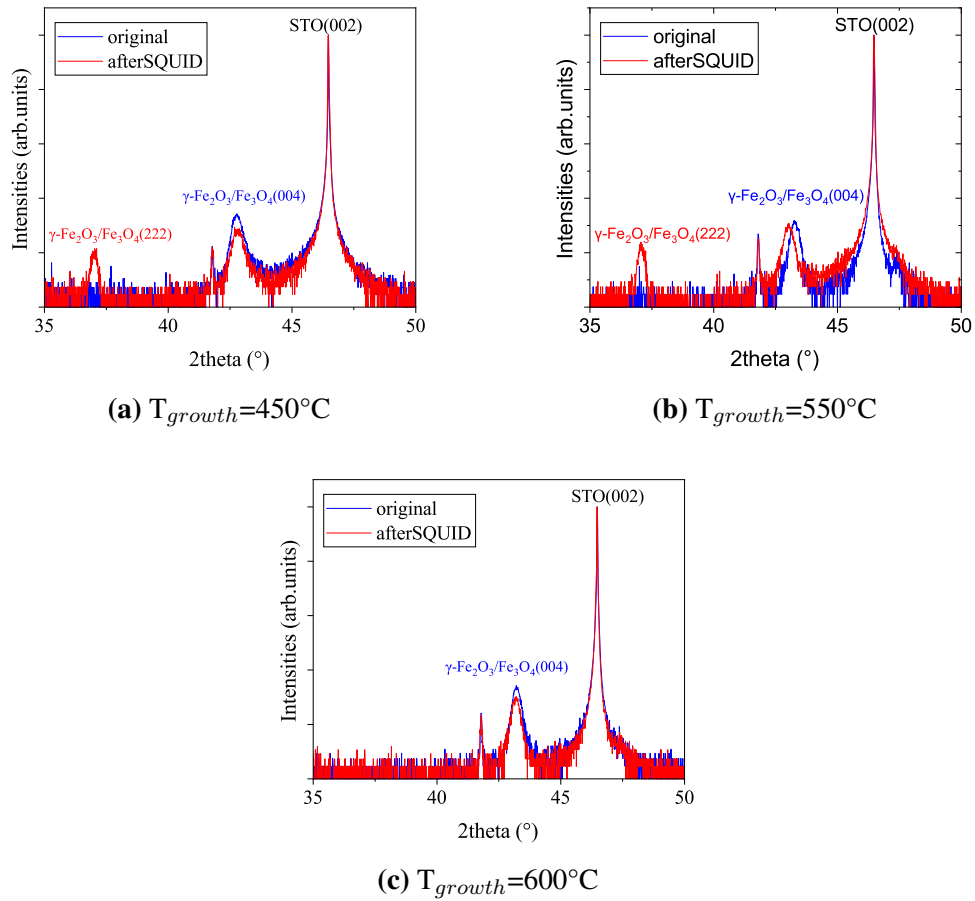


Figure 5.5: XRD images of $\text{Fe}_3\text{O}_4/\text{STO}$ before and after applying voltage in SQUID of samples grown at (a) 450°C , (b) 550°C , and (c) 600°C

Chapter 6

Summary

The aim of this project was to control and tune the phase and properties of iron oxide thin films on the Nb: STO substrates deposited by PLD. In my project thesis "Optimization of the growth conditions of magnetite films on YSZ substrates", we have managed to find the best laser fluency to grow Fe_3O_4 thin films which showed a relatively homogeneous surface with thickness around 40nm and good single crystallinity. Based on this laser fluency, we deposited Fe_3O_4 thin films on Nb: STO substrates using PLD.

First, we characterized the properties of Fe_3O_4 thin films grown at different growth temperatures. From AFM and XRR, we observed the relatively smooth surface with low roughness when $T_{growth} < 550^\circ\text{C}$ which indicates the good quality of thin films. From XRD measurements we observed only two peaks of Fe_3O_4 in the same direction of (004) which indicates single crystallinity. We observed the saturation magnetization lower than the bulk value because of the assumed presence of anti-phase boundaries. Using WAXS, we investigated the in-plane lattice constant of Fe_3O_4 which shows the same tendency as XRD. The Verwey transition temperature was calculated from the magnetization. As a good indicator of oxygen stoichiometry, we find that the Verwey transition temperature is lower than the bulk value which can be affected by the off-stoichiometry of thin films. Moreover, the Verwey transition temperature goes lower with increasing growth temperature, this indicates also different strain states for different growth temperatures.

After characterization of the Fe_3O_4 thin films, we used SQUID to tune the properties of thin films by applying voltage. By applying a positive voltage, we observed the disappearance of the Verwey transition. We assume that the oxygen anions are voltage driven to migrate from the substrate into the thin films. From ex-situ XRD, we observed

an additional peak, indicating the possible structural change or phase change in the thin film system.

Chapter 7

Outlook

We characterized the properties of Fe_3O_4 thin films and observed different strain and oxygen stoichiometry for different growth temperatures. In addition, we attempted to tune the properties of the Fe_3O_4 thin films by applying an electric field in a SQUID system.

As the crystal structure of $\gamma\text{-Fe}_2\text{O}_3$ is similar to Fe_3O_4 , we propose to further study the phase change in situ with applied voltage in X-ray magnetic circular dichroism (XMCD) and X-ray absorption spectra (XAS).

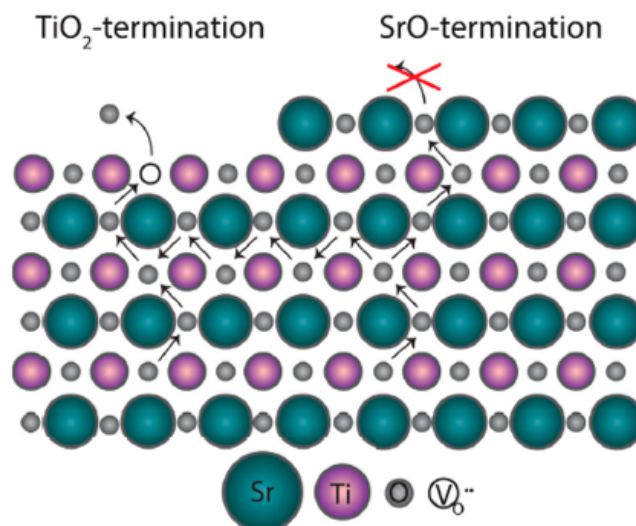


Figure 7.1: Different termination of STO substrate, figure taken from [5]

The lattice structure change with applied electric field will be observed by in-situ XRD and WAXS. Furthermore, with the help of Grazing-Incidence Wide-Angle X-ray Scattering (GIWAXS), we can study the influence of the surface and interface of thin film, separately.

The termination of STO has proved to play an important role in the oxygen migration kinetics [5]. As shown in fig.7.1, there are two kinds of termination on STO surfaces: SrO- and TiO₂-termination. Normally, the STO substrate is terminated with a mix of both terminations. With treatment, the TiO₂- or SrO-termination can be realized separately. The TiO₂- termination is more favorable to form oxygen vacancies, while the SrO-termination tends to form a barrier of oxygen vacancies and thus, completely suppresses the formation of oxygen vacancies. Thus, we will analyze the influence of oxide substrates on Fe₃O₄ thin films by using SrO terminated STO substrates as they have different oxygen supplying behaviour.

Appendix A

The calculation of WAXS data

The data collected by WAXS are saved to a mythen file. Each mythen file corresponds to one omega and includes a set of 2θ values and the corresponding intensities. In order to get the full information, we need to transform this data into ω and 2θ .

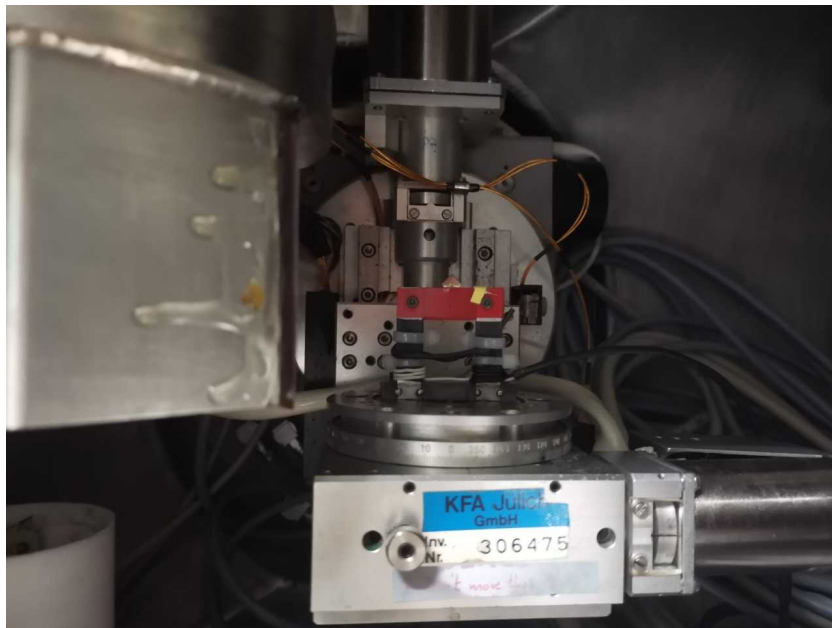


Figure A.1: Sample mounted in WAXS with $\text{PSR}=90^\circ$, $\omega_0=0^\circ$

Omega can be obtained from the number of mythen data and the starting angle and interval. In our experiment, the position of the sample rotator (PSR) starts from 90°

which corresponds to $\omega_0=0^\circ$. The starting PSR is shown in fig. A.1. The interval is kept to 0.01° . Thus the ω of i^{th} mythen can be represented as $\omega = 0.01 * i + \omega_0$. The 2θ value of each pixel can be calculated from the number of pixels. As shown in fig.3.10, the distance (D) from the sample to the middle of the detector is around 85mm. There are 1280 channels each $50\mu\text{m}$ in width and thus a detector length of 64mm. The angel between the incident beam and the middle of the diffracted beam is 2θ . The value of the *theta* is determined by the position of the detector and can be changed manually.

Taking the calculation in section 4.5 as an example: when we chose to observe the peaks around STO(113) peak, we can calculate the corresponding 2θ value by using Bragg's equation:

$$\lambda = 2d\sin\theta_0$$

$$d = \frac{a}{\sqrt{h^2 + k^2 + l^2}}$$

$$2\theta_0 = 2 * \arcsin\left(\frac{1.3414}{2 * \frac{3.911}{\sqrt{h^2+k^2+l^2}}}\right)$$

$$2\theta_0 = 69.3289^\circ$$

There are 48 score-marks around the circle with 7.5° in between where we can align the detector and decide the $2\theta_0$ value. In this situation we put the detector at scale 9 ($scale = 2\theta/7.5 \approx 9$). Then we can calculate the 2θ value of n^{th} channel of the detector:

$$\Delta = \arctan\left(\frac{\frac{640-n}{1280} * 64}{85}\right)$$

$$2\theta = 2\theta_0 - \Delta$$

Until now, we convert the mythen number and the detector channel position into ω and 2θ . In order to convert them into reciprocal space, we need to calculate the projection of Q which is Q_x and Q_z :

$$Q_x = \frac{2\pi}{\lambda} * (\cos(\omega) - \cos(2\theta - \omega))$$

$$Q_z = \frac{2\pi}{\lambda} * (\sin(\omega) + \sin(2\theta - \omega))$$

And we also know $Q = \frac{2\pi}{d}$, with the sample mounting in [110] direction which is introduced in Figure 4.6, we get:

$$Q_x = \frac{2\pi}{d_{hh0}} = \frac{2\pi * \sqrt{2} * h}{a_{ip}}$$

$$Q_z = \frac{2\pi}{d_{00l}} = \frac{2\pi * l}{c_{oop}}$$

Thus, we can calculate the h and l in the substrate unit:

$$h = \frac{Q_x * a_{ip}}{2\sqrt{2}\pi}$$

$$l = \frac{Q_z * c_{oop}}{2\pi}$$

The point which corresponds to the substrate peak will allocate on the integer. With the help of know the value of the reflection of each point (hkl), we can further calculate the in-plane and out-of-plane lattice constant: a_{ip} and c_{oop} :

$$a_{ip} = \frac{2\sqrt{2}\pi h}{Q_x}$$

$$c_{oop} = \frac{2\pi l}{Q_z}$$

Appendix B

Sources of systematic error in the WAXS system

The errors of the calculated data obtained from WAXS can be caused by different sources. The possible errors are shown in fig. B.1.

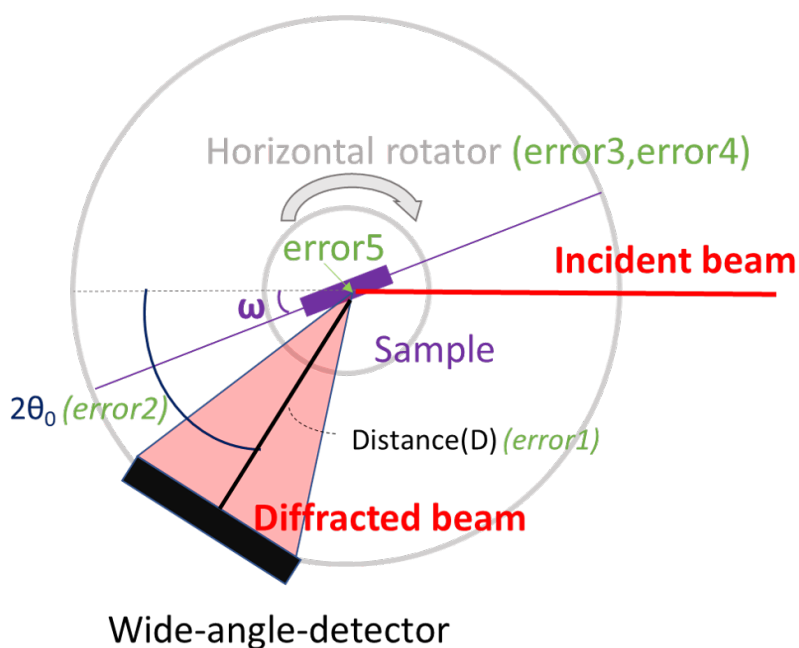


Figure B.1: 5 possible sources of error in WAXS system

1.) Distance between the sample and the detector: Different from SAXS, the distance should be 85mm, but there exists some deviation which makes this value only an approximation.

2.) The $2\theta_0$: Depending on the different peaks we need to observe, the $2\theta_0$ is defined manually according to the curve on the detector holder. This brings another error that needs to be corrected manually in the calculation.

3.) The ω_0 : The sample is mounted on the sample holder and parallel to the incident beam. At this time the position of the sample holder (PSR) should be 90° and the $\omega_0=0^\circ$. However, there exists some error which makes $\omega_0 \approx 0^\circ$.

4.) The speed of the sample rotator: At first, we keep the speed of the rotator as 200steps/sec as the grey curve in fig. B.2. In these circumstances we observe the instability of the substrate peak and the results are not perfectly reproducible. Then we reduced the motor speed to 100steps/sec, the substrate peak is still unrepeatabile. Then we reduced the motor speed to 50 steps/sec as the blue and green curves in fig. B.2. The shape and the intensities are very similar, thus, we eliminated the error induced by the motor speed. In our further study, we should keep the motor speed as 50 steps/sec.

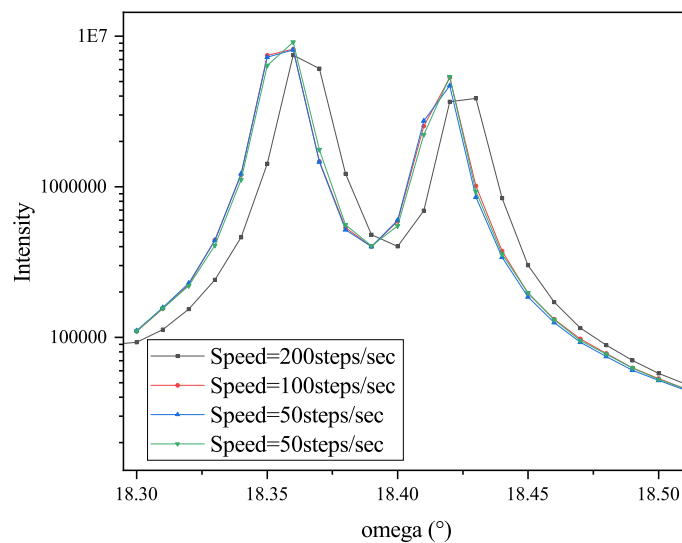


Figure B.2: Intensity integrated of all 2θ over ω

Error 5. The shift between the center of the sample and the center of rotation of the

detector: The detector is supposed to rotate around the center of the sample's rotation, which means that the center of ω and 2θ should be the same. But there exists a shift of the center of rotation of the detector from the center of the sample's rotation. This shift is around 2cm which also brings errors into the system. Recently, this shift has been resolved.

These uncertainties result in the errors of the calculation and are difficult to be adjusted with precision. How to obtain reasonable results with the help of eliminating the errors needs to be addressed in future measurements.

Bibliography

- [1] Ricardo Aragón, Douglas J Buttrey, John P Shepherd, and Jurgen M Honig. Influence of nonstoichiometry on the Verwey transition. *Physical Review B*, 31(1):430, 1985.
- [2] Artur Glavic. *Multiferroicity in oxide thin films and heterostructures*, volume 45. Forschungszentrum Jülich, 2012.
- [3] Quantum design. *Physical Property Measurement System Hardware Manual*.
- [4] Emmanuel Kentzinger, Margarita Krutyeva, and Ulrich Rücker. GALAXI: Gallium anode low-angle x-ray instrument. *Journal of large-scale research facilities JLSRF*, 2:61, 2016.
- [5] Felix VE Hensling, Christoph Baeumer, Marc-André Rose, Felix Gunkel, and Regina Dittmann. SrTiO₃ termination control: a method to tailor the oxygen exchange kinetics. *Materials Research Letters*, 8(1):31–40, 2020.
- [6] Malcolm W Chase. NIST-JANAF thermochemical tables for oxygen fluorides. *Journal of physical and chemical reference data*, 25(2):551–603, 1996.
- [7] Ze Zhang and Sashi Satpathy. Electron states, magnetism, and the Verwey transition in magnetite. *Physical Review B*, 44(24):13319, 1991.
- [8] Michail Fonin, Yu S Dedkov, Rossitza Pentcheva, Ulrich Rüdiger, and Gernot Güntherodt. Magnetite: a search for the half-metallic state. *Journal of Physics: Condensed Matter*, 19(31):315217, 2007.
- [9] RA De Groot, FM Mueller, PG Van Engen, and KHJ Buschow. New class of materials: half-metallic ferromagnets. *Physical Review Letters*, 50(25):2024, 1983.
- [10] S Blundell. Magnetism in condensed matter: oxford master series. *Condensed Matter Physics (Oxford Series Publications, 2001)*, page 29, 2001.

- [11] PW Anderson. Antiferromagnetism. Theory of superexchange interaction. *Physical Review*, 79(2):350, 1950.
- [12] Junjiro Kanamori. Superexchange interaction and symmetry properties of electron orbitals. *Journal of Physics and Chemistry of Solids*, 10(2-3):87–98, 1959.
- [13] John B Goodenough. Theory of the role of covalence in the perovskite-type manganites [La,M(II)]MnO₃. *Physical Review*, 100(2):564, 1955.
- [14] EJW Verwey. Electronic conduction of magnetite (Fe₃O₄) and its transition point at low temperatures. *Nature*, 144(3642):327–328, 1939.
- [15] EJW Verwey and EL Heilmann. Physical properties and cation arrangement of oxides with spinel structures I. cation arrangement in spinels. *The Journal of Chemical Physics*, 15(4):174–180, 1947.
- [16] Lo S Darken and RW Gurry. The system iron-oxygen. I. the wüstite field and related equilibria. *Journal of the American Chemical Society*, 67(8):1398–1412, 1945.
- [17] Robert M Hazen and Raymond Jeanloz. Wüstite (Fe_{1-x}O): A review of its defect structure and physical properties. *Reviews of Geophysics*, 22(1):37–46, 1984.
- [18] WL Roth. Defects in the crystal and magnetic structures of ferrous oxide. *Acta Crystallographica*, 13(2):140–149, 1960.
- [19] F Koch and JB Cohen. The defect structure of Fe_{1-x}O. *Acta Crystallographica Section B: Structural Crystallography and Crystal Chemistry*, 25(2):275–287, 1969.
- [20] J Willard Gibbs. The collected works of J. Willard Gibbs. Technical report, Yale Univ. Press., 1948.
- [21] Rochelle M Cornell and Udo Schwertmann. *The iron oxides: structure, properties, reactions, occurrences and uses*. John Wiley & Sons, 2003.
- [22] Mai Hussein Abdalla Hamed. Interface functionalization of magnetic oxide Fe₃O₄/SrTiO₃ heterostructures. Technical report, Elektronische Eigenschaften, 2021.
- [23] Ghenadii Korotcenkov. *The Future of Semiconductor Oxides in Next-Generation Solar Cells*. Elsevier, 2017.
- [24] EN Maslen, VA Streltsov, NR Streltsova, and NJAC Ishizawa. Synchrotron x-ray study of the electron density in α-Fe₂O₃. *Acta Crystallographica Section B: Structural Science*, 50(4):435–441, 1994.

- [25] Masashi Kawasaki, Kazuhiro Takahashi, Tatsuro Maeda, Ryuta Tsuchiya, Makoto Shinohara, Osamu Ishiyama, Takuzo Yonezawa, Mamoru Yoshimoto, and Hideomi Koinuma. Atomic control of the SrTiO₃ crystal surface. *Science*, 266(5190):1540–1542, 1994.
- [26] Jindong Li, Yanhe Liang, Jingyun Lv, Yiming Chai, and Sinan Li. The research progress of synthesis technology for Graphene/Fe₂O₃ composites. *Open Journal of Natural Science*, 8:379, 2020.
- [27] Richard D Leapman, LA Grunes, and PL Fejes. Study of the L₂₃ edges in the 3d transition metals and their oxides by electron-energy-loss spectroscopy with comparisons to theory. *Physical Review B*, 26(2):614, 1982.
- [28] K Van Benthem, C Elsässer, and RH French. Bulk electronic structure of SrTiO₃: Experiment and theory. *Journal of applied physics*, 90(12):6156–6164, 2001.
- [29] Takeshi Tomio, Hidejiro Miki, Hitoshi Tabata, Tomoji Kawai, and Shichio Kawai. Control of electrical conductivity in laser deposited SrTiO₃ thin films with nb doping. *Journal of Applied Physics*, 76(10):5886–5890, 1994.
- [30] A Hamie, Y Dumont, E Popova, A Fouchet, Bénédicte Warot-Fonrose, Christophe Gatel, E Chikoidze, J Scola, B Berini, and N Keller. Investigation of high quality magnetite thin films grown on SrTiO₃ (001) substrates by pulsed laser deposition. *Thin Solid Films*, 525:115–120, 2012.
- [31] S Celotto, W Eerenstein, and T Hibma. Characterization of anti-phase boundaries in epitaxial magnetite films. *The European Physical Journal B-Condensed Matter and Complex Systems*, 36(2):271–279, 2003.
- [32] T Hibma, FC Voogt, L Niesen, PAA Van der Heijden, WJM De Jonge, JJTM Donkers, and PJ Van der Zaag. Anti-phase domains and magnetism in epitaxial magnetite layers. *Journal of applied physics*, 85(8):5291–5293, 1999.
- [33] D Gilks, L Lari, K Matsuzaki, H Hosono, T Susaki, and VK Lazarov. Structural study of Fe₃O₄ (111) thin films with bulk like magnetic and magnetotransport behaviour. *Journal of Applied Physics*, 115(17):17C107, 2014.
- [34] Florencio Sanchez, Carmen Ocal, and Josep Fontcuberta. Tailored surfaces of perovskite oxide substrates for conducted growth of thin films. *Chemical Society Reviews*, 43(7):2272–2285, 2014.
- [35] M. Lippmaa, K. Takahashi, A. Ohtomo, S. Ohashi, T. Ohnishi, N. Nakagawa, T. Sato, M. Iwatsuki, H. Koinuma, and M. Kawasaki. Atom technology for josephson tunnel junctions: SrTiO₃ substrate surface. *Materials Science and Engineering: B*, 56(2):111–116, 1998.

-
- [36] David Nečas and Petr Klapetek. Gwyddion: an open-source software for SPM data analysis. *Open Physics*, 10(1):181–188, 2012.
- [37] Heinz Kiessig. Untersuchungen zur Totalreflexion von Röntgenstrahlen. *Annalen der Physik*, 402(6):715–768, 1931.
- [38] Matts Björck and Gabriella Andersson. Genx: an extensible X-ray reflectivity refinement program utilizing differential evolution. *Journal of Applied Crystallography*, 40(6):1174–1178, 2007.
- [39] Giorgio Bertotti. *Hysteresis in magnetism: for physicists, materials scientists, and engineers*. Gulf Professional Publishing, 1998.
- [40] VAM Brabers, F Walz, and H Kronmüller. Impurity effects upon the Verwey transition in magnetite. *Physical Review B*, 58(21):14163, 1998.
- [41] Michael A Green. Residual fields in superconducting magnets. In *Proceedings of the MT-4 Conference at Brookhaven National Laboratory*, volume 339, 1972.
- [42] Amit Kumar and S.M. Yusuf. The phenomenon of negative magnetization and its implications. *Physics Reports*, 556:1–34, 2015. The phenomenon of negative magnetization and its implications.